

Equivariant Symmetry-Aware Head Pose Estimation for Fetal MRI

Ramya Muthukrishnan¹, Borjan Gagoski², Aryn Lee², P. Ellen Grant²,
Elfar Adalsteinsson¹, Polina Golland¹, Benjamin Billot³

¹MIT CSAIL

²Boston Children’s Hospital, Harvard Medical School

³Inria, Sophia Antipolis

¹{ramyamut,elfar,polina}@mit.edu,

²{borjan.gagoski, aryn.lee,ellen.grant}@childrens.harvard.edu, ³bbillot@inria.fr

Abstract

We present *E(3)-Pose*, a novel fast pose estimation method that jointly and explicitly models rotation equivariance and object symmetry. Our work is motivated by the challenging problem of accounting for fetal head motion during a diagnostic MRI scan. We aim to enable automatic adaptive prescription of 2D diagnostic MRI slices with 6-DoF head pose estimation, supported by 3D MRI volumes rapidly acquired before each 2D slice. Existing methods struggle to generalize to clinical volumes, due to pose ambiguities induced by inherent anatomical symmetries, as well as low resolution, noise, and artifacts. In contrast, *E(3)-Pose* captures anatomical symmetries and rigid pose equivariance by construction, and yields robust estimates of the fetal head pose. Our experiments on publicly available and representative clinical fetal MRI datasets demonstrate the superior robustness and generalization of our method across domains. Crucially, *E(3)-Pose* achieves state-of-the-art accuracy on clinical MRI volumes, supporting future clinical translation. Our implementation is publicly available¹.

1. Introduction

Real-time 6-DoF object pose estimation enables a wide range of critical navigation tasks in robotic manipulation [2], autonomous driving [8], and image-guided surgery [77]. Here, we present a novel method for rapid object pose estimation from 3D images based on an architecture that captures pose equivariance and object symmetries by construction. We are motivated by the problem of motion estimation in fetal

MRI, where stacks of 2D diagnostic MRI slices are acquired to assess fetal development and detect pathology [22, 23] (Appendix A). Due to inter-slice fetal motion, oblique slices and spatial coverage gaps in the acquired stack present challenges to radiological assessment and often necessitate re-acquisition of the entire stack [47, 71, 76]. One solution is to estimate the fetal head pose from rapid, low-resolution, low signal-to-noise ratio (SNR) 3D MRI “navigator” volumes inserted into the MRI sequence before every 2D slice. The aim is to use the pose estimated from each navigator volume to adaptively adjust the imaging plane of the next slice (Fig. 1) [17, 29, 65]. Estimating fetal head pose from navigator volumes is particularly challenging. In addition to low resolution and SNR, these volumes contain an imaging artifact that presents as a dark plane in the position of the previous (high energy) slice and may obstruct relevant anatomical features (e.g., eyes) that are crucial for pose disambiguation. Moreover, underdeveloped neuroanatomy coupled with low resolution creates an approximate left-right symmetry, introducing pose ambiguities [78]. Finally, the lack of available navigator data necessitates training on higher resolution, higher SNR, artifact-free research volumes, thus creating cross-domain generalization challenges.

Several existing methods detect pre-specified anatomical landmarks to compute pose [32, 63], but landmark visibility is not guaranteed in clinical data. Another class of methods formulates the problem as rigid registration of a moving volume to a template [4, 51, 67]. However, in navigator volumes, artifacts perturb the intensity distributions of moving volumes relative to the template, leading to suboptimal registration. Canonical pose regression with convolutional neural networks (CNNs) can improve robustness to reduced anatomical visibility and imaging artifacts [19, 59, 74]. Despite their benefits, these methods are prone to overfitting even with data augmentations, and are highly sensitive to pose ambiguities.

Contributions. We propose *E(3)-Pose*, a novel framework

¹Code: <https://github.com/MedicalVisionGroup/E3-Pose>
Project page: ramyamut.github.io/e3-pose

This work is supported by the the MIT Abdul Latif Jameel Clinic, the MIT-Takeda Program, the Chou Family Transformative Research Fund, NIH NIBIB (R01EB032708, ST32EB1680), and NIH NICHD (R01HD100009). This work involved human subjects or animals in its research. Approval of all ethical and experimental procedures and protocols was granted by the Institutional Review Board of Boston Children’s Hospital.

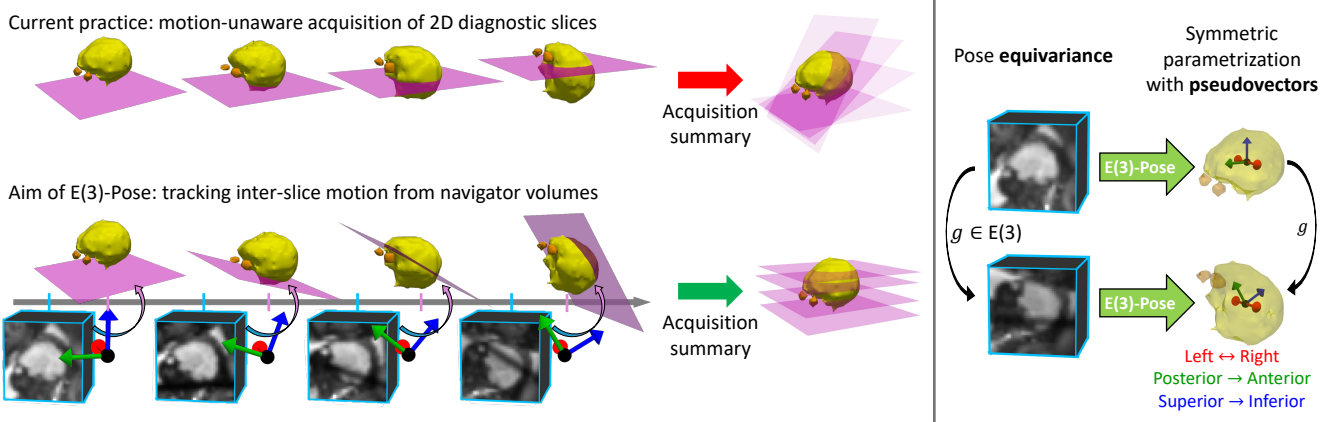


Figure 1. **E(3)-Pose is a rotation-equivariant and symmetry-aware framework for 6-DoF pose estimation.** *Left:* a rapid navigator volume is inserted between every two 2D diagnostic MRI slices. Our aim is to estimate the fetal head pose to adjust imaging plane prescription in real time. *Right:* To enable robust performance, the network architecture employs E(3)-equivariant convolutional filters to capture pose equivariance and pseudovectors to account for left-right head symmetry.

for accurate and generalizable head pose estimation from fetal brain volumes (Fig. 1). In contrast to standard convolutions that are by construction only equivariant to translations, we leverage an E(3)-equivariant CNN (E(3)-CNN) for pose regression to also account for rotation equivariance [20, 70]. Moreover, we use pseudovectors [28] in the learned equivariant rotation parametrization to model left-right head symmetry. E(3)-Pose achieves competitive performance on publicly available research-quality datasets, and state-of-the-art performance on *clinically* representative datasets. Crucially, our experiments demonstrate that constraining the network architecture to explicitly model physical symmetries provides better generalization to out-of-distribution data and stabilizes pose estimates in ambiguous cases with low anatomical visibility. Overall, while this paper focuses on fetal MRI, our method holds promise for object localization tasks that involve symmetries, limited training data, and real-world applications with noisy sensors.

2. Related work

Landmark-based pose estimation. Landmark registration involves algorithmic detection of pre-defined anatomical structures to estimate pose relative to a canonical anatomical frame [30, 32, 63]. To mitigate dependence on visibility of specific anatomy, recent approaches trained a neural network to learn an overcomplete set of landmarks [4, 66]. Nevertheless, learned landmarks display sensitivity to perturbations of volume intensities, posing problems when fast acquisitions introduce disruptive artifacts. In contrast, we directly regress pose, circumventing these challenges.

Pose regression. Early pose regression approaches relied on rotation parametrizations that suffer from discontinuities over SO(3), such as axis-angle vectors [25, 59]. It has

been shown that high-dimensional, continuous parametrizations offer smoother loss landscapes and robustness to noise [21, 81]. Existing methods that adopt this strategy regress two basis directions [15, 81] or a deformation field [24] of the canonical object frame relative to the input volume. E(3)-Pose similarly regresses a continuous, overcomplete parametrization by using three basis directions.

Equivariant networks. A function is equivariant under a group of transforms if it commutes with every transform in the group. In the context of CNNs, standard convolutions are already equivariant under translations. There has been significant progress toward convolutions that are equivariant under a broader group, including SE(3) and E(3) [10–12, 20, 64, 69, 70, 73]. Specifically, these architectures restrict the space of learnable parameters to those that strictly adhere to inherent symmetries, rather than learning equivariance through data augmentation. Theoretical analysis shows that equivariant architectures are more sample-efficient, reducing overfitting especially when training data is limited [5, 40, 60]. By leveraging an E(3)-equivariant CNN for pose estimation, E(3)-Pose robustly generalizes to noisy clinical data.

Existing equivariant methods for 6-DoF pose estimation either predict the relative transform between image pairs [4, 43, 51, 68, 79] or formulate rotation estimation as a classification problem over a discretized set of 3D rotations [7, 34, 42, 45, 52]. Furthermore, these methods do not explicitly account for symmetric ambiguities in their network architectures. In contrast, E(3)-Pose regresses a continuous output over SO(3) and handles object symmetry in the construction of this parametrization.

Object symmetries. Rotational and reflectional object symmetries can lead to pose ambiguities. One class of solutions trains a network to implicitly learn object symmetries via

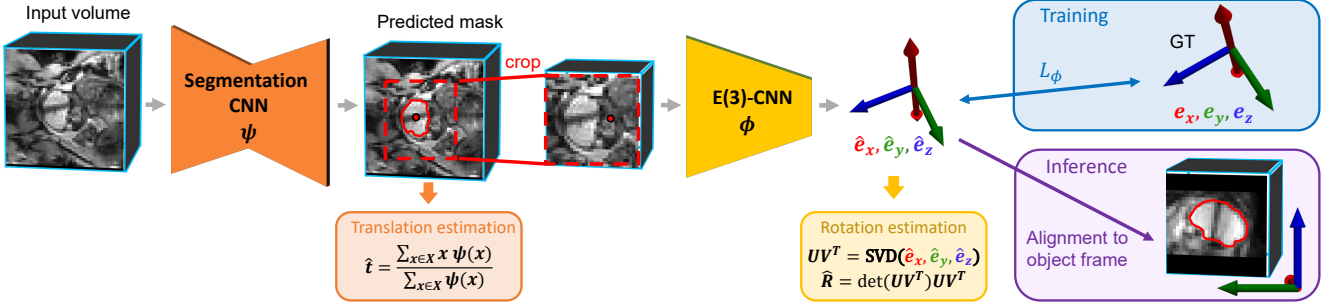


Figure 2. **Overview of E(3)-Pose.** We first train a CNN ψ to segment the object. We estimate translation based on the center-of-mass of the predicted mask and then crop the 3D volumes around this mask using a 40% margin. The cropped volumes are fed to an E(3)-CNN ϕ trained independently to regress the orthonormal basis of the object frame, parametrized as one pseudovector (red) and two vectors (blue and green). The output is later constrained to represent a rotation matrix by applying SVD and then choosing the pseudovector \hat{e}_x direction that results in a proper rotation without reflection (i.e., $\det(M(\hat{R})) = 1$).

probabilistic outputs, and heuristically selects the most probable pose during inference [31, 80]. Yet, these methods suffer from discontinuities in the network output over the object symmetry group [57]. Although training with symmetry-invariant losses partially alleviates this problem [74], these discontinuities are more robustly eliminated by incorporating object symmetry into the pose parametrization itself. Namely, this strategy regresses an output that remains *invariant* under the object symmetry group, while maintaining continuity over the group of all non-symmetric input transformations [54, 57, 61]. To handle head pose ambiguities, E(3)-Pose models the basis direction along the axis of left-right symmetry as a pseudovector [28], which maintains both invariance under left-right reflections and continuity over SO(3). While pseudovectors have been used to model rotation axes in pose estimation [41], our method is the first to use them to address symmetric ambiguities.

Automated slice prescription in fetal brain MRI. Existing implementations use the pose estimated from a single volume acquired at the start of the sequence to prescribe all slices in the stack [32, 63]. While this approach accurately prescribes slices according to the initial head pose, it does not account for inter-slice motion. In contrast, E(3)-Pose aims to adjust the imaging plane for every slice in the stack, based on the head pose estimated from the preceding navigator volume.

3. Preliminaries

In this section, we provide context for E(3)-Pose by introducing key theoretical concepts in the design of E(3)-CNNs.

Tensor fields and E(3) representations. Let $f: \mathbb{R}^3 \rightarrow \mathbb{R}^d$ be a d -dimensional tensor field. Consider 3D Euclidean group actions $g = g_t \circ g_r$, which comprise rotations/reflections $g_r \in \text{O}(3)$ and translations $g_t \in \mathbb{R}^3$. When the coordinate system is transformed by g , the tensor $f(x)$ at point $x \in \mathbb{R}^3$ is modified in two ways: it is moved to the location $g^{-1}x$ and the tensor

is independently rotated/reflected by g_r [20, 70]. Formally, we can define an operator $[\pi_f(g)f](x) = \rho_f(g_r)f(g^{-1}x)$ that transforms field f for any $g = g_t \circ g_r \in \text{E}(3)$. In this formulation, $\rho_f: \text{O}(3) \rightarrow \mathbb{R}^{d \times d}$ is called a *representation*; it is a matrix acting linearly on the tensor space of $f(x)$ that describes how the tensor independently transforms under g_r .

Irreducibility. A representation ρ and the tensors it transforms are *irreducible* if there is no change of basis $Q \in \mathbb{R}^{d \times d}$ such that $Q\rho(g_r)Q^{-1}$ is block-diagonal for all $g_r \in \text{O}(3)$. Irreducible representations and tensors are characterized by order l and parity, defining how $f(x)$ transforms under proper rotations and inversion (i.e., reflection across all three planes) of the coordinate system, respectively [20]. Even parity indicates no change in $f(x)$ under inversion, while odd parity indicates a sign change in $f(x)$. While one can define tensors and representations of any order and parity, we focus here on three types: first, scalars $f(x) \in \mathbb{R}$ (order $l = 0$, even parity) have representation $\rho_{\text{even}}^{l=0}(g_r) = 1$; second, vectors $f(x) \in \mathbb{R}^3$ ($l = 1$, odd parity) have representation $\rho_{\text{odd}}^{l=1}(g_r) = M(g_r)$, where $M: \text{O}(3) \rightarrow \mathbb{R}^{3 \times 3}$ is the matrix representation of an orthogonal transformation; and last, pseudovectors $f(x) \in \mathbb{R}^3$ ($l = 1$, even parity) have representation $\rho_{\text{even}}^{l=1}(g_r) = (\det M(g_r))M(g_r)$ with a positive determinant to account for invariance under inversion [28].

Equivariance. Let F be a mapping between two tensor fields f and h associated with operators π_f and π_h and representations ρ_f and ρ_h , respectively. F is equivariant under $\text{E}(3)$ if and only if

$$F(\pi_f(g)f) = \pi_h(g)F(f), \text{ for all } g \in \text{E}(3). \quad (1)$$

A similar relation holds if F is a function mapping tensor field f to a single tensor h with representation ρ_h :

$$F(\pi_f(g)f) = \rho_h(g_r)F(f), \text{ for all } g = g_t \circ g_r \in \text{E}(3). \quad (2)$$

Equivariant networks. E(3)-CNNs can be built using successive equivariant layers, since their composition remains

equivariant. Here we describe equivariant convolutional layers (see Appendix B for pooling and non-linearities). For enhanced computation and time efficiency, state-of-the-art implementations of such CNNs operate on irreducible fields [20, 70]. Let $\kappa_{l_f p_f, l_h p_h}(x) \in \mathbb{R}^{(2l_h+1) \times (2l_f+1)}$ be a 3D convolution kernel transforming field f (order l_f , parity p_f) to field h (order l_h , parity p_h). Then, κ must satisfy Eq. (1) to maintain equivariance, resulting in the solution

$$\text{vec}(\kappa_{l_f p_f, l_h p_h}(x)) = \sum_{m \in M} \sum_{j \in J} w_{jm} \varphi_m(\|x\|) Q_j Y_j(x/\|x\|), \quad (3)$$

where vec indicates vectorization, w_{jm} are coefficients, $\{\varphi_m\}$ are radially symmetric basis functions, $Q_j \in \mathbb{R}^{(2l_h+1)(2l_f+1) \times (2j+1)}$ are changes of basis, $Y_j : S^2 \rightarrow \mathbb{R}^{2j+1}$ are the degree- j spherical harmonics, and $J = \{j : |l_f - l_h| \leq j \leq |l_f + l_h|, j \text{ is even}\}$ if $p_f = p_h$ or $J = \{j : |l_f - l_h| \leq j \leq |l_f + l_h|, j \text{ is odd}\}$ if $p_f \neq p_h$ [20, 70]. E(3)-CNNs are thus trained by learning the coefficients w_{jm} rather than the kernel values themselves.

4. Methods

Our goal is to estimate a 6-DoF canonical object pose T from a 3D volume, with respect to the volume coordinate frame. We estimate the rigid pose $T = t \circ R$ by separating it into its rotation R and translation t components (Fig. 2).

4.1. Translation estimation

In rigid pose estimation, it is customary to place the origin of the object coordinate frame at the object center [74]. If $\psi : \mathbb{R}^3 \rightarrow \{0, 1\}$ is a binary object occupancy function, then t can be computed from a set X of sampled points (i.e., voxel coordinates): $t = \frac{\sum_{x \in X} x \psi(x)}{\sum_{x \in X} \psi(x)}$. See Appendix C for our implementation of ψ using a CNN for fetal brain segmentation from whole-uterus MRI volumes.

4.2. Rotation estimation

Function equivariance. We first define $f : \mathbb{R}^3 \rightarrow \mathbb{R}$ as the scalar field representing the input volume, with transformation operator $[\pi_f(g)f](x) = f(g^{-1}x)$; $h(R) \in \mathbb{R}^d$ as some d -dimensional tensor parametrization of the output rotation R , with representation ρ_h ; and $\phi : f \rightarrow h$ as the rotation estimation function. Rotating/reflecting the input volume rotates/reflects its pose equivalently, requiring function equivariance detailed in Eq. (2):

$$\phi(f \circ g^{-1}) = \rho_h(g_r) \phi(f), \quad \text{for all } g = g_t \circ g_r \in \text{E}(3). \quad (4)$$

Although in practice we require equivariance under $\text{SE}(3)$ rather than the full group $\text{E}(3)$, we show below that using an E(3)-CNN to implement ϕ enables us to jointly formulate $h(R)$ as equivariant under $\text{SE}(3)$ and invariant under left-right reflections. Since E(3)-CNNs must operate on

irreducible tensors, it suffices to parametrize $h(R)$ with irreducible tensors to guarantee the equivariance of ϕ .

Rotation parametrization. Let $G_{\text{symm}} = \{g_s \in \text{O}(3) : f \circ g_s^{-1} = f\}$ be the object symmetry group [61]. To handle object symmetries, we aim to parametrize $h(R)$ such that $\rho_h(g_s)h(R) = h(R)$ for all $g_s \in G_{\text{symm}}$ and $R \in \text{SO}(3)$; and h remains continuous over $\text{SO}(3)$. Here, we consider the case $G_{\text{symm}} = \{g_{\leftrightarrow}\}$, where g_{\leftrightarrow} denotes left-right reflection, defined by the axis of left-right symmetry e_{\leftrightarrow} .

Formally, we define $h(R)$ based on three orthonormal basis directions $\{e_x, e_y, e_z\}$ of the object frame ($d=9$):

$$\begin{aligned} h(R) &= e_x \oplus e_y \oplus e_z, \\ \text{s.t. } e_x &= e_{\leftrightarrow} \text{ and } e_y, e_z \perp e_{\leftrightarrow}, \\ \rho_h(g_r) &= (\det M(g_r)) M(g_r) \oplus M(g_r) \oplus M(g_r) \\ &= \rho_{\text{even}}^{l=1}(g_r) \oplus \rho_{\text{odd}}^{l=1}(g_r) \oplus \rho_{\text{odd}}^{l=1}(g_r), \end{aligned} \quad (5)$$

where \oplus denotes columnwise/block-diagonal concatenation for vectors/matrices, respectively. Specifically, we decompose $h(R)$ into three irreducible tensors: a *pseudovector* parametrizes the left-right direction, and two vectors parametrize two directions orthogonal to the left-right axis. Invariance under G_{symm} is straightforward:

$$\begin{aligned} \rho_h(g_{\leftrightarrow})h(R) &= (\det M(g_{\leftrightarrow})) M(g_{\leftrightarrow}) e_x \oplus M(g_{\leftrightarrow}) e_y \oplus M(g_{\leftrightarrow}) e_z, \\ &= (\det M(g_{\leftrightarrow})) (-e_x) \oplus e_y \oplus e_z \\ &= e_x \oplus e_y \oplus e_z = h(R), \end{aligned} \quad (6)$$

where the second equality follows from the fact that following reflection, vectors orthogonal to the reflection axis are unchanged, and those that are parallel become inverted. Since we use an E(3)-CNN to estimate $h(R)$, we ensure that $h(R)$ is equivariant under $\text{SE}(3) \subset \text{E}(3)$. ρ_h is essentially the rotation matrix when group actions are restricted to $\text{SO}(3)$, establishing the continuity of h over $\text{SO}(3)$.

E(3)-CNN regressor. To handle both rotational equivariance and reflectional symmetry, we implement ϕ as an E(3)-CNN regressor taking a scalar field as input, and returning an output tensor that decomposes into one pseudovector \hat{e}_x and two vectors \hat{e}_y, \hat{e}_z , normalized to unit length. Appendix B provides a detailed description of the network architecture. During training, we minimize the objective function

$$\mathcal{L}_{\phi} = |\sin(\theta_x)| + \beta(|\sin(\theta_y/2)| + |\sin(\theta_z/2)|), \quad (7)$$

where (e_x, e_y, e_z) is the ground-truth (GT) orthonormal basis, $\theta_k = \arccos(\hat{e}_k \cdot e_k)$ for $k \in \{x, y, z\}$, and β is a weight hyperparameter. Our loss function is invariant under G_{symm} (Appendix D). During inference, we obtain an orthonormal output matrix by applying SVD to the predicted basis [44]. We then choose between \hat{e}_x and $-\hat{e}_x$ in order to guarantee a positive determinant matrix, i.e., a proper rotation. This step is related to prior work that heuristically selects the output

pose from a set of symmetrically plausible poses [31, 54, 80]. Here, the task is straightforward since we are choosing between a right-handed and left-handed rotation.

4.3. Implementation details

Object frame. We place the origin of the target object frame at the center-of-mass (CoM) of the brain. We define the GT orthonormal basis e_x , e_y , and e_z as the unit vectors pointing along the left→right (L→R), posterior→anterior (P→A), and inferior→superior (I→S) anatomical orientations of the brain, respectively (Fig. 2). This follows Eq. (5), where e_x is parallel and e_y , e_z are orthogonal to the left-right axis, respectively. See Appendix E for details.

Data augmentation. We augment training volumes with commonly used spatial (rigid transformations, scaling, flips) and intensity (bias field, gamma, Gaussian noise, low resolution) transforms [3, 55] in volumetric brain MRI. To enable our method to generalize to navigator volumes interleaved with diagnostic slices, we additionally simulate a spin history artifact from the preceding slice [17, 49], which appears as dark shading along the slice imaging plane (blue arrows in Fig. 3). We model this artifact with a Gaussian approximation of the slice profile $\tilde{f}(x) = f(x)(1 - \mathcal{N}((x - c_{\text{slice}})^T n_{\text{slice}}; 0, \sigma^2))$, where f and \tilde{f} are the original and augmented volumes, respectively; c_{slice} and n_{slice} are the center and normal to the slice imaging plane, sampled uniformly at random; and σ^2 is determined by slice thickness and the rate of spin decay [39] (see Appendix F for more details).

5. Experiments and results

5.1. Data

We train two variants of E(3)-Pose on two different large, high-quality *research* datasets. We first evaluate on in-distribution held-out test data. Then, we evaluate on two *clinical* datasets to assess domain generalization and the potential for clinical translation. All volumes are annotated for ground-truth pose and segmentations (Appendix G).

Research. We train one instance of E(3)-Pose on **Research-Fetal**, a dataset of 3D whole-uterus MRI volumes in 153 pregnant volunteers acquired at the Boston Children’s Hospital. We train another instance of our method on **dHCP**, a publicly available dataset of fetal brain MRI scans in 245 volunteers [36]. Fetus gestational age (GA) is 18-38 and 20-38 weeks in Research-Fetal and dHCP, respectively. All volumes have 2-3mm isotropic voxels. They are not interleaved with diagnostic slices and do not contain spin history artifacts. We use training/validation/testing splits of 114/15/25 and 148/48/49 participants for Research-Fetal and dHCP, respectively. dHCP consists of higher quality volumes, presenting a more challenging clinical domain generalization task compared to Research-Fetal. Additionally, dHCP vol-

umes are neatly cropped around the fetal head. Therefore, segmentation networks trained on dHCP fail to accurately predict the brain mask in volumes where the field of view is larger and includes uterine regions outside the head and maternal tissues (Fig. 3). For this reason, we train our segmentation network only on Research-Fetal.

Clinical. We evaluate the methods on **Clinical-Young**, a dataset of routine clinical volumes in 60 *younger* fetuses (GA 18-23 weeks). This dataset presents two challenges: clinical volumes exhibit a substantial domain shift from high-quality research data, and underdeveloped anatomy complicates pose estimation [78]. The voxel size is 1.76-3.5mm, and volumes are not interleaved with diagnostic slices. We also test the models on **Navigators**, a dataset containing 47 time-series (1210 total volumes) of 3D MRI navigator volumes interleaved with 2D slices in 9 volunteers (GA 26-36 weeks). Due to fast and interleaved acquisitions, these volumes have voxel size 4-6mm and contain real spin history artifacts. This dataset represents the largest domain gap from the research data, and volumes are representative of the intended clinical application, i.e., adaptive slice prescription. Both clinical datasets are acquired at the Boston Children’s Hospital.

5.2. Evaluation metrics

We assess performance with the geodesic rotation error $\arccos(\frac{1}{2}[\text{trace}(R\hat{R}^{-1}) - 1])$ and the average absolute distance (AAD) for voxels on the brain surface [26] (see Appendix I for additional metrics).

5.3. Baseline methods

Template-based. We evaluate two baseline methods that perform rigid registration to a template volume. FireANTs [35] is a state-of-the-art method for fast, optimization-based 3D image registration. EquiTrack [4] uses a SE(3)-equivariant network that learns matching landmarks to compute the optimal rigid transform from the input to the template via SVD [44]. To enable comparison with E(3)-Pose, we generate subject-specific template volumes using the GT pose. For accurate registration, we mask input volumes with the brain masks predicted by our segmentation network.

Template-free. We evaluate four baseline methods that estimate the canonical pose from only the input volume. Fetal-Align [32] implements landmark-based pose estimation, which segments the brain and eyes as landmarks and uses brain shape to resolve left-right ambiguity. For fair comparison on our datasets, we use our trained segmentation network, which we train to segment both the brain and eyes, to perform landmark detection. The remaining three baselines directly regress pose with CNNs. 3DPose-Net [59] and 6DRep [15] regress the axis-angle vector and two basis directions of the object frame, respectively. The latter method applies Gram-Schmidt orthonormalization [83] to

Table 1. **Baseline comparisons.** Mean \pm standard deviation for rotation error ($^{\circ}$) and average absolute error (AAD, mm). Best score is in bold. * indicates statistical significance at $p < 0.05$ compared to E(3)-Pose (hierarchical permutation test for Navigators, pairwise Wilcoxon for all other datasets). FireANTs and Fetal-Align are not re-trained for rotation estimation; we report the performance statistics separately for these methods. FireANTs runtime is 1.8s, prohibiting real-time deployment. EquiTrack runtime is 0.7s, and the remaining methods run in 0.3s. See Tables 4-5 for subject-level statistics in Navigators.

	Research-Fetal test		dHCP test		Clinical-Young		Navigators	
	Rot. error	AAD	Rot. error	AAD	Rot. error	AAD	Rot. error	AAD
FireANTs [35]	10.6 \pm 24.5*	5.7 \pm 9.3*	0.4 \pm 1.6*	0.6 \pm 1.0*	17.3 \pm 40.6	4.1 \pm 7.4	44.6 \pm 55.6*	19.1 \pm 20.3*
Fetal-Align [32]	5.0 \pm 3.0	3.0 \pm 1.7	8.5 \pm 24.7*	3.5 \pm 6.8*	10.3 \pm 21.0*	3.2 \pm 5.0*	56.2 \pm 57.6*	24.1 \pm 23.3*
Trained on Research-Fetal								
EquiTrack [4]	11.3 \pm 13.1*	6.2 \pm 5.9*	7.1 \pm 5.0	3.6 \pm 2.6	18.9 \pm 29.0*	5.4 \pm 5.7*	44.7 \pm 48.7*	20.3 \pm 18.3*
3DPose-Net [59]	19.8 \pm 15.0*	10.5 \pm 7.6*	24.0 \pm 19.2*	10.9 \pm 7.5*	39.2 \pm 36.8*	11.2 \pm 8.6*	65.0 \pm 47.8*	27.7 \pm 16.3*
6DRep [15]	9.6 \pm 4.5*	5.3 \pm 2.3*	9.8 \pm 5.5*	4.9 \pm 3.0*	14.1 \pm 7.7*	4.6 \pm 2.3*	38.8 \pm 45.7*	17.2 \pm 15.9*
RbR [24]	7.6 \pm 3.9*	4.3 \pm 2.2*	8.6 \pm 5.0	4.3 \pm 2.6	11.2 \pm 4.6*	3.7 \pm 1.4*	22.6 \pm 24.1*	11.5 \pm 9.9*
E(3)-Pose (ours)	5.1 \pm 2.6	3.0 \pm 1.7	7.4 \pm 3.6	3.7 \pm 1.8	9.1 \pm 4.7	3.0 \pm 1.4	9.4 \pm 7.5	6.3 \pm 4.0
Trained on dHCP								
EquiTrack [4]	29.5 \pm 43.5*	14.1 \pm 19.5*	13.6 \pm 36.7*	5.4 \pm 11.6*	48.3 \pm 62.1*	11.6 \pm 13.2*	59.0 \pm 57.5*	25.7 \pm 22.1*
3DPose-Net [59]	33.5 \pm 26.6*	17.1 \pm 11.6*	21.2 \pm 27.4*	9.0 \pm 8.9*	51.5 \pm 37.8*	14.4 \pm 8.9*	93.9 \pm 55.8*	36.2 \pm 16.7*
6DRep [15]	32.2 \pm 26.0*	17.3 \pm 14.2*	12.2 \pm 6.1*	5.9 \pm 3.1*	48.2 \pm 50.8*	12.4 \pm 10.8*	84.1 \pm 51.2*	34.0 \pm 17.3*
RbR [24]	15.4 \pm 18.3*	8.3 \pm 8.5*	8.0 \pm 4.0*	3.9 \pm 1.9	50.9 \pm 48.4*	12.7 \pm 9.9*	77.2 \pm 53.6*	30.8 \pm 17.3*
E(3)-Pose (ours)	5.7 \pm 3.6	3.4 \pm 2.0	7.3 \pm 3.4	3.7 \pm 1.7	12.1 \pm 6.8	3.9 \pm 1.9	13.9 \pm 13.2	7.9 \pm 5.6

the network output to obtain the final rotation. Registration-by-Regression (RbR) [24] trains a U-Net to regress a deformation field of the object frame at the same resolution as the input volume. The final rotation is computed from the network output with SVD [33]. We train all three networks on the research datasets and tune augmentation parameters for optimal performance. To run full rigid pose estimation for these methods, which estimate rotation only, we use CoM-based translation estimation. Appendix H provides further details on the baseline methods.

5.4. Results

We first evaluate performance on in-domain research data, and then assess generalization to target clinical domains. Table 1 reports the performance statistics on the test volumes from each dataset, and Fig. 3 shows example alignments.

Research. E(3)-Pose accurately predicts pose and significantly outperforms other direct pose regression methods, showcasing the advantage of modeling rotational equivariance. E(3)-Pose is outperformed by template-based methods on dHCP test data, where the intensity distribution of the input volume is similar to the template at higher resolution and SNR, eliminating alignment ambiguities. Here, template registration is able to effectively exploit the information advantage of a subject-specific template *aligned to the GT pose*. The accuracy of Fetal-Align indicates that precise landmark detection supports reliable computation of the head pose, consistent with our landmark-based GT pose definition (Appendix E).

Clinical-Young. E(3)-Pose yields accurate pose estimates in clinical acquisitions of younger ages, outperforming all

baseline methods. This difference is more pronounced when training on dHCP, which consists of higher-SNR volumes and presents an even larger distribution shift from clinical data compared to Research-Fetal. E(3)-Pose is the only method that maintains its performance in both training settings, highlighting the robust generalization advantages of our method. For further insight, we study the performance as a function of GA. Fig. 4 reveals that template-based methods (FireANTs and EquiTrack) break down on younger fetuses, where underdeveloped, spherical brain shapes and the lack of structure differentiation within the brain [78] lead to alignment ambiguities (Fig. 3). 6DRep and RbR remain relatively stable across GAs when trained on Research-Fetal: by removing dependence on specific anatomical markers, direct pose regression is less sensitive to the lack of fine-grained details. However, pose regression with standard CNNs struggles to generalize to younger GAs when trained on dHCP, suggesting that these methods are prone to overfitting to the training distribution. In contrast, E(3)-Pose provides accurate results across GAs and training datasets.

Navigators. E(3)-Pose achieves accurate pose estimation in navigator volumes and significantly outperforms all baselines (Table 1). While all baseline methods struggle with the challenging task of generalizing from dHCP to Navigators, E(3)-Pose remains robust to the substantial domain gap. Importantly, E(3)-Pose successfully recovers head pose even in volumes with high uncertainty, which occur when the effects of low resolution, low SNR, and artifact obstruction combine to eliminate most asymmetric cues (Fig. 3, columns 4-6). In contrast, template registration methods are prone to errors when spin history artifacts disrupt the similarity

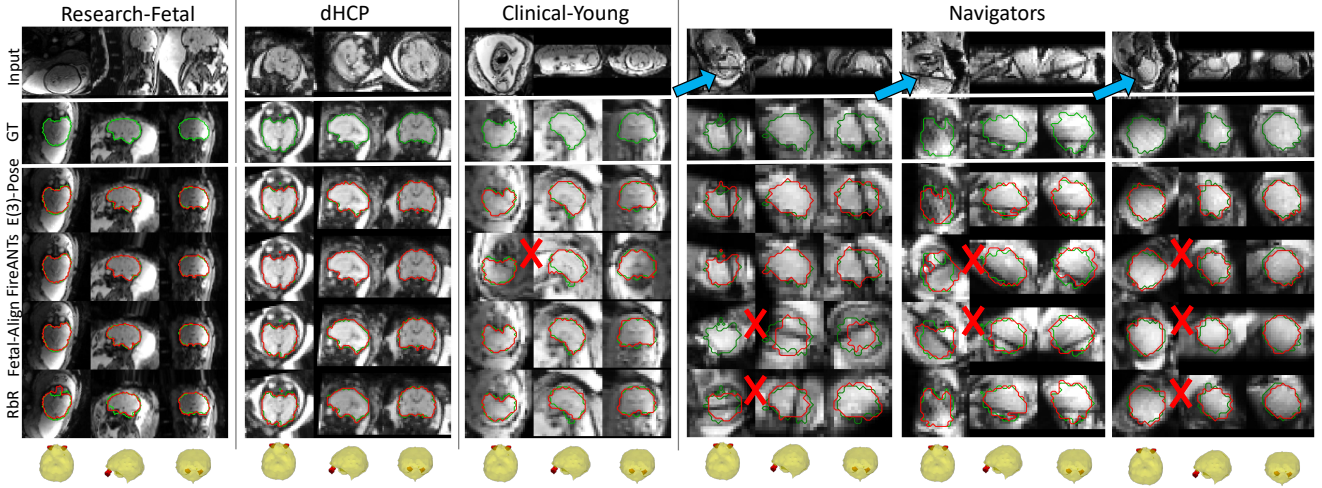


Figure 3. Example results for methods trained on Research-Fetal. Volumes are displayed before (row 1) and after (rows 2-6) alignment to the canonical object frame. The brain mask is also aligned to the GT (green outline) and predicted (red outline) frames. Navigator volumes include spin history artifacts (blue arrows) and low resolution/SNR, posing challenges for pose estimation. While baseline methods struggle (red Xs, rotation error $> 60^\circ$) in younger fetuses (column 3) and navigator volumes (columns 4-6), E(3)-Pose correctly predicts pose in all cases. E(3)-Pose remains accurate under significant pose ambiguity, e.g. when the artifact intersects both eyes, large voxel size obscures brain structure, and the fetal brain is close to a sphere (column 6).

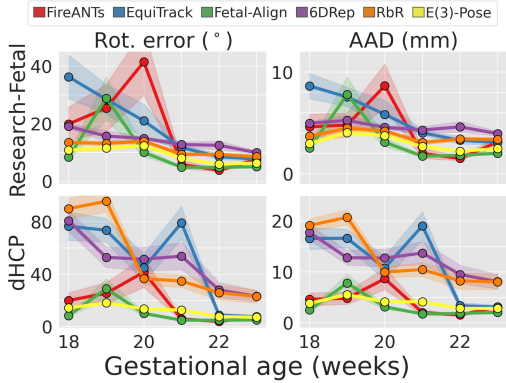


Figure 4. Clinical-Young results. Performance statistics are shown as a function of gestational age for all well-performing methods trained on Research-Fetal (top) and dHCP (bottom).

between input and template intensity distributions, and Fetal-Align remains highly sensitive to eye visibility, which is often limited by artifact obstruction or blurring due to voxel size. Moreover, E(3)-Pose generally yields more stable estimates compared to CNN-based pose regression, highlighting that enforcing pose equivariance and anatomical symmetry on the network parameters is an effective regularization technique that enables generalization to out-of-distribution clinical volumes and stability under pose ambiguity.

5.5. Ablation study

To study performance on challenging out-of-distribution cases, we evaluate ablations on clinical datasets (Table 2).

Appendix K provides results on research datasets, and Fig. 13 provides example alignments.

Equivariance. We ablate the modeling of rotational pose equivariance by replacing all E(3)-equivariant convolutions with standard convolutions equivariant to only translations. The results show that rotation equivariance is critical for generalization to clinical data, especially when the domain gap between training and testing data is significant. This outcome is in line with prior work [5, 40, 60] and our comparison to non-equivariant RbR, 6DRep, and 3DPose-Net.

Rotation parametrization. We consider alternative equivariant rotation parametrizations. First, we study the impact of estimating a symmetry-invariant parametrization by replacing the pseudovector with a standard vector. Table 2 shows that E(3)-Pose significantly outperforms this ablation, which struggles under pose ambiguities. Second, we reduce the dimensionality of the rotation parametrization by predicting only two basis directions: e_y and e_z . We observe that estimating a third basis direction significantly reduces errors in challenging clinical volumes.

Loss function and data augmentation. We now examine the effect of two alternative loss functions that are not invariant under left-right reflections (Appendix K). We first train our network by replacing the pseudovector loss term in Eq. (7) with that of the standard vectors. Next, we replace our objective with the widely used geodesic loss [59]. Table 2 shows that both loss functions significantly reduce performance in Navigators, emphasizing the importance of combin-

Table 2. **Ablation study.** Mean \pm standard deviation statistics for rotation error ($^\circ$) and average absolute error (AAD, mm). Best score is in bold. * indicates statistical significance compared to E(3)-Pose at $p < 0.05$ compared to E(3)-Pose (hierarchical permutation test for Navigators, pairwise Wilcoxon for all other datasets). See Tables 7-8 for subject-level statistics in Navigators.

	Trained on Research-Fetal				Trained on dHCP			
	Clinical-Young		Navigators		Clinical-Young		Navigators	
	Rot. error	AAD	Rot. error	AAD	Rot. error	AAD	Rot. error	AAD
E(3)-Pose (ours)	9.1 ± 4.7	3.0 ± 1.4	9.4 ± 7.5	6.3 ± 4.0	12.1 ± 6.8	3.9 ± 1.9	13.9 ± 13.2	7.9 ± 5.6
Standard CNN	$10.3 \pm 5.4^*$	$3.4 \pm 1.5^*$	$18.0 \pm 19.3^*$	$9.7 \pm 7.6^*$	$53.3 \pm 55.8^*$	$12.9 \pm 11.9^*$	$80.2 \pm 52.7^*$	$31.9 \pm 17.3^*$
no pseudovector	$10.4 \pm 4.0^*$	$3.4 \pm 1.3^*$	$10.9 \pm 11.1^*$	$7.0 \pm 5.0^*$	12.1 ± 7.7	3.9 ± 2.2	$20.6 \pm 26.1^*$	$10.6 \pm 10.1^*$
$h(R) = e_y \oplus e_z$	$10.3 \pm 4.2^*$	$3.4 \pm 1.3^*$	$11.9 \pm 12.9^*$	$7.3 \pm 5.5^*$	11.6 ± 6.5	3.7 ± 1.8	$26.1 \pm 35.6^*$	$12.3 \pm 12.2^*$
$\mathcal{L}_\phi = \sum_{k \in \{x, y, z\}} \sin(\theta_k/2) $	8.8 ± 3.6	3.0 ± 1.3	$12.1 \pm 11.1^*$	$7.2 \pm 5.1^*$	11.1 ± 5.3	3.6 ± 1.5	18.5 ± 27.3	9.4 ± 9.4
geodesic loss	9.2 ± 4.7	3.1 ± 1.5	$13.5 \pm 20.0^*$	$9.7 \pm 7.6^*$	30.9 ± 53.4	7.7 ± 10.9	$27.8 \pm 42.5^*$	$12.6 \pm 14.0^*$
no artifact augmentation	12.0 ± 21.1	3.5 ± 3.8	$16.2 \pm 18.6^*$	$7.7 \pm 7.6^*$	$18.4 \pm 21.1^*$	$5.4 \pm 4.5^*$	$31.9 \pm 36.7^*$	$15.1 \pm 13.9^*$

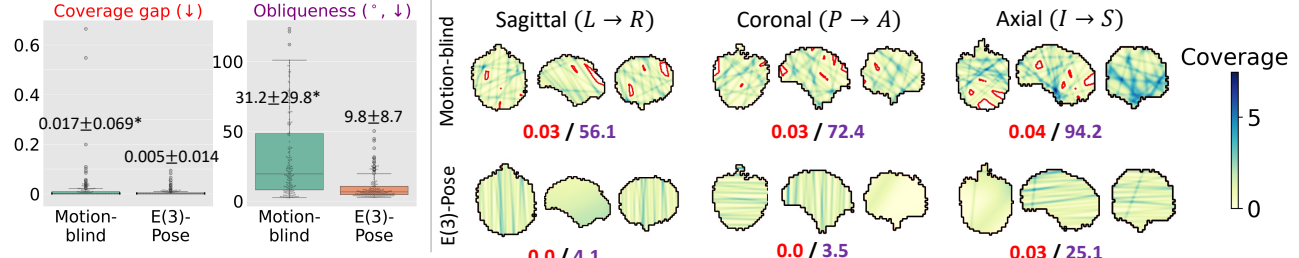


Figure 5. **Simulation results.** *Left:* Quantitative comparison of diagnostic slice stacks obtained using motion-blind prescription and E(3)-Pose. Mean \pm standard deviation statistics are displayed. * indicates statistical significance ($p < 0.05$, pairwise Wilcoxon). *Right:* Brain coverage of the slice stacks prescribed by each method, for three different example subjects and target anatomical orientations. Coverage gap (red) and obliqueness (purple, $^\circ$) metrics are respectively displayed. Spatial coverage gap regions are outlined in red.

ing both symmetry-invariant architectures and loss functions for stable performance under high ambiguity. Lastly, ablating the simulated spin history artifact during training shows that this augmentation critically enables generalization to Navigators, where volumes contain real spin history artifacts.

5.6. Simulation study

We further establish the clinical utility of E(3)-Pose through simulations of automated slice prescription, using test volumes from Research-Fetal. We simulate stacks of slices in the sagittal ($L \rightarrow R$), coronal ($P \rightarrow A$), and axial ($I \rightarrow S$) orientations in all subjects. We compare our method to a “motion-blind” strategy, which prescribes every slice based on the fetal head pose in the first navigator volume only. We assess the quality of the simulated stacks by computing the coverage gap (i.e., the ratio of brain volume that is not captured) and slice obliqueness (i.e., rotation error between the prescribed and target slice orientations). Appendix L provides implementation details and additional evaluations. Fig. 5 shows that E(3)-Pose yields significant improvements in both metrics. Under motion-blind prescription, large inter-slice motion leads to oblique slices that frequently intersect, producing highly uneven spatial coverage and, in the worst cases, complete coverage gaps. In contrast, E(3)-Pose adaptively adjusts the imaging plane to follow the movements

of the head. Our approach prescribes parallel slices closely aligned to the target anatomical orientation, improving the coverage uniformity and reducing the likelihood of coverage gaps in our simulations.

6. Discussion and Conclusion

We present E(3)-Pose, a novel framework for 6-DoF pose estimation. By jointly modeling rigid pose equivariance and reflectional object symmetry, E(3)-Pose enables robust generalization to challenging domains with pose ambiguities.

Our symmetry assumption, which is only an approximation based on the low resolution of navigator volumes, may break under large lateralized pathology. In these cases, the three-vector variant of E(3)-Pose, which does not assume left-right symmetry, may be more robust. In addition, E(3)-Pose does not explicitly model motion history or identify high-uncertainty cases, both of which could help to mitigate errors in noisy clinical volumes. Future work will investigate equivariant approaches for estimating probability distributions over $SO(3)$, conditioned on motion trajectories [38, 56]. See Appendix M for further discussion of limitations.

In our experiments, we provide the first evaluation on data representative of clinical applications in fetal brain MRI, bringing the promise of clinical deployment closer to reality.

References

[1] Kathy Ayala, Christina Huynh, Kristin Voegtle, and Helena JV Rutherford. Made to move: A review of measurement strategies to characterize heterogeneity in normal fetal movement. *Infant Behavior and Development*, 75:101949, 2024. 4

[2] Aude Billard and Danica Kragic. Trends and challenges in robot manipulation. *Science*, 364(6446):eaat8414, 2019. 1

[3] Benjamin Billot, Douglas N. Greve, Oula Puonti, Axel Thielscher, Koen Van Leemput, Bruce Fischl, Adrian V. Dalca, and Juan Eugenio Iglesias. SynthSeg: segmentation of brain MRI scans of any contrast and resolution without retraining. *Medical Image Analysis*, 86:102789, 2023. 5

[4] Benjamin Billot, Neel Dey, Daniel Moyer, Malte Hoffmann, Esra Abaci Turk, Borjan Gagoski, P. Ellen Grant, and Polina Golland. SE(3)-equivariant and noise-invariant 3D rigid motion tracking in brain MRI. *IEEE Transactions on Medical Imaging*, 43(11):4029–4040, 2024. 1, 2, 5, 6, 4

[5] Srinath Bulusu, Matteo Favoni, Andreas Ipp, David I. Müller, and Daniel Schuh. Equivariance and generalization in neural networks. *EPJ Web of Conferences*, 258:09001, 2022. 2, 7

[6] Shulei Cai, Guofu Zhang, He Wang, and Jing Wang. Normative linear and volumetric biometric measurements of fetal brain development in magnetic resonance imaging. *Child's Nervous System*, 36:2997–3005, 2020. 1

[7] Haiwei Chen, Shichen Liu, Weikai Chen, Hao Li, and Randall Hill. Equivariant point network for 3D point cloud analysis. In *Proceedings of the IEEE/CVF Conference on Computer Vision and Pattern Recognition (CVPR)*, pages 14514–14523, 2021. 2

[8] Hsu-Kuang Chiu, Jie Li, Rareş Ambruş, and Jeannette Bohg. Probabilistic 3D multi-modal, multi-object tracking for autonomous driving. In *2021 IEEE International Conference on Robotics and Automation (ICRA)*, pages 14227–14233, 2021. 1

[9] Djork-Arné Clevert, Thomas Unterthiner, and Sepp Hochreiter. Fast and accurate deep network learning by exponential linear units (ELUs). *arXiv: Learning*, 2015. 3

[10] Taco S. Cohen and Max Welling. Group equivariant convolutional networks. *Proc. Int. Conf. Mach. Learn.*, pages 2990–2999, 2016. 2

[11] Taco S. Cohen and Max Welling. Steerable CNNs. In *Int. Conf. Learn. Rep.*, 2017.

[12] Taco S. Cohen, Mario Geiger, Jonas Köhler, and Max Welling. Spherical CNNs. In *Int. Conf. Learn. Rep.*, 2018. 2

[13] Ivan Diaz, Mario Geiger, and Richard Iain McKinley. Leveraging SO(3)-steerable convolutions for pose-robust semantic segmentation in 3D medical data. *Machine Learning for Biomedical Imaging*, 2:834–855, 2024. 2, 3

[14] Sebastian Diaz, Benjamin Billot, Neel Dey, Molin Zhang, Esra Abaci Turk, P. Ellen Grant, Polina Golland, and Elfar Adalsteinsson. Robust fetal pose estimation across gestational ages via cross-population augmentation. In *Medical Image Computing and Computer Assisted Intervention – MICCAI 2025: 28th International Conference, Daejeon, South Korea, September 23–27, 2025, Proceedings, Part VII*, page 549–559, Berlin, Heidelberg, 2025. Springer-Verlag. 10

[15] Razieh Faghihpirayesh, Davood Karimi, Deniz Erdogmus, and Ali Gholipour. Automatic brain pose estimation in fetal MRI. In *Medical Imaging 2023: Image Processing*, page 124640T. International Society for Optics and Photonics, SPIE, 2023. 2, 5, 6, 7

[16] Martin A. Fischler and Robert C. Bolles. Random sample consensus: a paradigm for model fitting with applications to image analysis and automated cartography. *Communications of the ACM*, 24(6):381–395, 1981. 6

[17] Borjan Gagoski, Patrick McDaniel, André J. W. van der Kouwe, Himanshu Bhat, Lawrence L. Wald, Elfar Adalsteinsson, P. Ellen Grant, and M. Dylan Tisdall. HASTE imaging with EPI volumetric navigators for real-time fetal head motion detection. *Proc. Intl. Soc. Magn. Reson. Med.*, 2016. 1, 5

[18] Fei Gao, Hyunsoo Yoon, Teresa Wu, and Xianghua Chu. A feature transfer enabled multi-task deep learning model on medical imaging. *Expert Systems with Applications*, 143: 112957, 2020. 3

[19] Ge Gao, Mikko Lauri, Yulong Wang, Xiaolin Hu, Jianwei Zhang, and Simone Frintrop. 6D object pose regression via supervised learning on point clouds. In *2020 IEEE International Conference on Robotics and Automation (ICRA)*, pages 3643–3649, 2020. 1

[20] Mario Geiger and Tess Smidt. e3nn: Euclidean neural networks, 2022. 2, 3, 4, 11

[21] A. René Geist, Jonas Frey, Mikel Zobro, Anna Levina, and Georg Martius. Learning with 3D rotations: a hitchhiker's guide to SO(3). In *Proceedings of the 41st International Conference on Machine Learning*. JMLR.org, 2024. 2

[22] Ali Gholipour, Judith A. Estroff, Carol E. Barnewolt, Richard L. Robertson, P. Ellen Grant, Borjan Gagoski, Simon K. Warfield, Onur Afacan, Susan A. Connolly, Jeffrey J. Neil, Adam Wolfberg, and Robert V. Mulkern. Fetal MRI: a technical update with educational aspirations, 2014. 1

[23] Orit A. Glenn. MR imaging of the fetal brain. *Pediatr Radiol*, 40:68–81, 2009. 1

[24] Karthik Gopinath, Xiaoling Hu, Malte Hoffmann, Oula Puonti, and Juan Eugenio Iglesias. Registration by regression (RBR): a framework for interpretable and flexible atlas registration. *Biomed. Image Regist. Proc.*, 90:205–215, 2025. 2, 6, 5, 7

[25] F. Sebastian Grassia. Practical parameterization of rotations using the exponential map. *J. Graph. Tools*, 3(3):29–48, 1998. 2

[26] Douglas N. Greve and Bruce Fischl. Accurate and robust brain image alignment using boundary-based registration. *NeuroImage*, 48(1):63–72, 2009. 5

[27] K. M. Górska, E. Hivon, A. J. Banday, B. D. Wandelt, F. K. Hansen, M. Reinecke, and M. Bartelmann. HEALPix: a framework for high-resolution discretization and fast analysis of data distributed on the sphere. *The Astrophysical Journal*, 622(2):759, 2005. 11

[28] Walter Hauser. Vector products and pseudovectors. *Am. J. Phys.*, 54:168–172, 1986. 2, 3

[29] Aaron T. Hess, M. Dylan Tisdall, Ovidiu C. Andronesi, Ernesta M. Meintjes, and André J. W. van der Kouwe. Real-time motion and B0 corrected single voxel spectroscopy using

volumetric navigators. *Magnetic Resonance in Medicine*, 66(2):314–323, 2011. 1

[30] Derek L. G. Hill, Philipp G. Batchelor, Mark Holden, and David J. Hawkes. Medical image registration. *Phys. Med. Biol.*, 46(3), 2001. 2

[31] Tomáš Hodaň, Dániel Baráth, and Jiří Matas. EPOS: Estimating 6D pose of objects with symmetries. *IEEE Conference on Computer Vision and Pattern Recognition (CVPR)*, 2020. 3, 5

[32] Malte Hoffmann, Esra Abaci Turk, Borjan Gagoski, Leah Morgan, Paul Wighton, M. Dylan Tisdall, Martin Reuter, Elfar Adalsteinsson, P. Ellen Grant, Lawrence L. Wald, and André J W van der Kouwe. Rapid head-pose detection for automated slice prescription of fetal-brain MRI. *Int. J. Imaging. Syst. Technol.*, 31(3):1136–1154, 2021. 1, 2, 3, 5, 6

[33] Berthold Horn. Closed-form solution of absolute orientation using unit quaternions. *Journal of the Optical Society*, 4:629–642, 1987. 6

[34] Owen Howell, David Klee, Ondrej Biza, Linfeng Zhao, and Robin Walters. Equivariant single view pose prediction via induced and restriction representations. In *Advances in Neural Information Processing Systems*, pages 47251–47263. Curran Associates, Inc., 2023. 2

[35] Rohit Jena, Pratik Chaudhari, and James C Gee. FireANTS: Adaptive riemannian optimization for multi-scale diffeomorphic registration. *arXiv preprint arXiv:2404.01249*, 2024. 5, 6, 4

[36] Vyacheslav R. Karolis, Lucilio Cordero-Grande, Anthony N. Price, Emer Hughes, Sean P. Fitzgibbon, Vanessa Kyriakopoulou, Alena Uus, Nicholas Harper, Denis Prokopenko, Devi Bridglal, Jucha Willers Moore, Sian Wilson, Maximilian Pietsch, Daan Christiaens, Maria Deprez, Logan Z.J. Williams, Emma C. Robinson, Antonis Makropoulos, Seyedeh-Rezvan Farahibozorg, Jonathan O’Muircheartaigh, Mary A. Rutherford, Daniel Rueckert, A. David Edwards, Tomoki Arichi, Stephen M. Smith, Eugene Duff, and Joseph V. Hajnal. The developing human connectome project fetal functional MRI release: methods and data structures. *Imaging Neuroscience*, 3, 2025. 5, 4

[37] Diederik P. Kingma and Jimmy Ba. Adam: a method for stochastic optimization. In *Int. Conf. Learn. Rep.*, 2015. 3

[38] David M Klee, Ondrej Biza, Robert Platt, and Robin Walters. Image to sphere: learning equivariant features for efficient pose prediction. In *International Conference on Learning Representations*, 2023. 8

[39] Maria Kuklisova-Murgasova, Gerardine Quaghebeur, Mary A. Rutherford, Joseph V. Hajnal, and Julia A. Schnabel. Reconstruction of fetal brain MRI with intensity matching and complete outlier removal. *Medical Image Analysis*, 16(8):1550–1564, 2012. 5, 10

[40] Hannah Lawrence, Kristian Georgiev, Andrew Dienes, and Bobak T Kiani. Implicit bias of linear equivariant networks. *Int. Conf. Mach. Learn.*, 2022. 2, 7

[41] Byung-Hun Lee, Sung-Mo Kang, and Hyo-Sung Ahn. Distributed orientation estimation in $SO(d)$ and applications to formation control and network localization. *IEEE Transactions on Control of Network Systems*, 6(4):1302–1312, 2019. 3

[42] Jongmin Lee and Minsu Cho. 3D equivariant pose regression via direct wigner-D harmonics prediction. In *Advances in Neural Information Processing Systems*, pages 127765–127798. Curran Associates, Inc., 2024. 2, 11

[43] Jongmin Lee, Byungjin Kim, and Minsu Cho. Self-supervised equivariant learning for oriented keypoint detection. In *Proceedings of the IEEE/CVF Conference on Computer Vision and Pattern Recognition (CVPR)*, pages 4847–4857, 2022. 2

[44] Jake Levinson, Carlos Esteves, Kefan Chen, Noah Snavely, Afshin Rostamizadeh Angjoo Kanazawa, and Ameesh Makadia. An analysis of SVD for deep rotation estimation. In *Advances in Neural Information Processing Systems 34*, 2020. To appear in. 4, 5

[45] Xiaolong Li, Yijia Weng, Li Yi, Leonidas J Guibas, A. Abbott, Shuran Song, and He Wang. Leveraging $SE(3)$ equivariance for self-supervised category-level object pose estimation from point clouds. In *Advances in Neural Information Processing Systems*, pages 15370–15381. Curran Associates, Inc., 2021. 2

[46] Annemarie B Lüchinger, Mijna Hadders-Algra, Colette M van Kan, and Johanna I P de Vries. Fetal onset of general movements. *Pediatric Research*, 63(2):191–195, 2008. 4

[47] C. Malamateneiou, S.J. Malik, S.J. Counsell, J.M. Allsop, A.K. McGuinness, T. Hayat, K. Broadhouse, R.G. Nunes, A.M. Ederies, J.V. Hajnal, and M.A. Rutherford. Motion-compensation techniques in neonatal and fetal MR imaging. *American Journal of Neuroradiology*, 34(6):1124–1136, 2013. 1

[48] J Matas, O Chum, M Urban, and T Pajdla. Robust wide-baseline stereo from maximally stable extremal regions. *Image and Vision Computing*, 22(10):761–767, 2004. British Machine Vision Computing 2002. 6

[49] Karla L. Miller, Andreas J. Bartsch, and Stephen M. Smith. Simultaneous multi-slice imaging for resting-state fMRI. *Magnetom Flash*, 63(3):389–399, 2015. 5

[50] Fausto Milletari, Nassir Navab, and Seyed-Ahmad Ahmadi. V-Net: fully convolutional neural networks for volumetric medical image segmentation. In *Fourth Int. Conf. 3D Vision*, pages 565–571, 2016. 3

[51] Daniel Moyer, Esra Abaci Turk, P. Ellen Grant, William M. Wells, and Polina Golland. Equivariant filters for efficient tracking in 3D imaging. In *Medical Image Computing and Computer Assisted Intervention – MICCAI 2021*, pages 193–202, Cham, 2021. Springer International Publishing. 1, 2

[52] Mohamed Adel Musallam, Vincent Gaudilli  re, Miguel Ortiz del Castillo, Kassem Al Ismaeil, and Djamilia Aouada. Leveraging equivariant features for absolute pose regression. In *Proceedings of the IEEE/CVF Conference on Computer Vision and Pattern Recognition (CVPR)*, pages 6876–6886, 2022. 2

[53] Ramya Muthukrishnan, Paul Wighton, Robert Frost, André J. W. van der Kouwe, Aryn P. Lee, Elfar Adalsteinsson, P. Ellen Grant, Polina Golland, and Borjan Gagoski. Towards real-time navigation in diagnostic fetal brain MRI. *Proc. Int. Soc. Magn. Reson. Med.*, 2026. 1

[54] Giorgia Pitteri, Micha  l Ramamonjisoa, Slobodan Ilic, and Vincent Lepetit. On object symmetries and 6D pose estimation from images. *CoRR*, abs/1908.07640, 2019. 3, 5

[55] Fernando Pérez-García, Rachel Sparks, and Sébastien Ourselin. TorchIO: a python library for efficient loading, preprocessing, augmentation and patch-based sampling of medical images in deep learning. *Computer Methods and Programs in Biomedicine*, 208:106236, 2021. [5](#) [3](#)

[56] Arun Srivatsan Rangaprasad, Gillian Rosen, Drqaid Hadi, and Howie Choset. Estimating SE(3) elements using a dual quaternion based linear kalman filter. In *Robotics: Science and Systems (RSS)*, 2016. [8](#)

[57] Jesse Richter-Klug and Udo Frese. Handling object symmetries in CNN-based pose estimation. In *2021 IEEE International Conference on Robotics and Automation (ICRA)*, pages 13850–13856, 2021. [3](#)

[58] Francois Rousseau, Orit A. Glenn, Bistra Iordanova, Claudia Rodriguez-Carranza, Daniel B. Vigneron, James A. Barkovich, and Colin Studholme. Registration-based approach for reconstruction of high-resolution *in utero* fetal MR brain images. *Academic Radiology*, 13(9):1072–1081, 2006. [10](#)

[59] Seyed S.M. Salehi, Shadab Khan, Deniz Erdogmus, and Ali Gholipour. Real-time deep pose estimation with geodesic loss for image-to-template rigid registration. *IEEE Trans. Med. Imag.*, 38(2):470–481, 2019. [1](#) [2](#) [5](#) [6](#) [7](#)

[60] Akiyoshi Sannai, Masaaki Imaizumi, and Makoto Kawano. Improved generalization bounds of group invariant / equivariant deep networks via quotient feature spaces. In *Conference on Uncertainty in Artificial Intelligence*, 2019. [2](#) [7](#)

[61] Ashutosh Saxena, Justin Driemeyer, and Andrew Y. Ng. Learning 3-D object orientation from images. In *Proceedings of the 2009 IEEE International Conference on Robotics and Automation*, page 4266–4272. IEEE Press, 2009. [3](#) [4](#)

[62] Ken Shoemake. Animating rotation with quaternion curves. In *Proceedings of the 12th Annual Conference on Computer Graphics and Interactive Techniques*, page 245–254, New York, NY, USA, 1985. Association for Computing Machinery. [10](#)

[63] Sara Neves Silva, Sarah McElroy, Jordina Aviles Verdera, Kathleen Colford, Kamilah St Clair, Raphael Tomi-Tricot, Alena Uus, Valéry Ozenne, Megan Hall, Lisa Story, Kuberan Pushparajah, Mary A. Rutherford, Joseph V. Hajnal, and Jana Hutter. Fully automated planning for anatomical fetal brain MRI on 0.55T. *Magn. Reson. Med.*, 92(3):1263–1276, 2024. [1](#) [2](#) [3](#)

[64] Nathaniel Thomas, Tess E. Smidt, Steven Kearnes, Lusann Yang, Li Li, Kai Kohlhoff, and Patrick Riley. Tensor field networks: Rotation- and translation-equivariant neural networks for 3D point clouds. *CoRR*, abs/1802.08219, 2018. [2](#)

[65] M. Dylan Tisdall, Aaron T. Hess, Martin Reuter, Ernesta M. Meintjes, Bruce Fischl, and André J. W. van der Kouwe. Volumetric navigators for prospective motion correction and selective reacquisition in neuroanatomical MRI. *Magn. Reson. Med.*, 68(2):389–399, 2012. [1](#)

[66] Alan Q. Wang, Evan M. Yu, Adrian V. Dalca, and Mert R. Sabuncu. A robust and interpretable deep learning framework for multi-modal registration via keypoints. *Medical Image Analysis*, 90:102962, 2023. [2](#)

[67] Jian Wang, Razieh Faghihpirayesh, Polina Golland, and Ali Gholipour. SpaER: learning spatio-temporal equivariant representations for fetal brain motion tracking. In *Perinatal, Preterm and Paediatric Image Analysis*, pages 3–13, Cham, 2025. Springer Nature Switzerland. [1](#)

[68] Rui Wang, Rose Yu, and Robin Walters. Approximately equivariant networks for imperfectly symmetric dynamics. In *Int. Conf. Mach. Learn.*, 2022. [2](#) [11](#)

[69] Maurice Weiler and Gabriele Cesa. General E(2)-Equivariant Steerable CNNs. In *Conference on Neural Information Processing Systems (NeurIPS)*, 2019. [2](#)

[70] Maurice Weiler, Mario Geiger, Max Welling, Wouter Boomsma, and Taco Cohen. 3D steerable CNNs: learning rotationally equivariant features in volumetric data. *Proc. Adv. Neural Inf. Process. Systems*, 31, 2018. [2](#) [3](#) [4](#) [11](#)

[71] Nathan White, Cooper Roddey, Ajit Shankaranarayanan, Eric Han, Dan Rettmann, Juan Santos, Josh Kuperman, and Anders Dale. PROMO: real-time prospective motion correction in MRI using image-based tracking. *Magn. Reson. Med.*, 61(3):91–105, 2010. [1](#)

[72] Paul Wighton, Oliver Hinds, Robert Frost, Malte Hoffmann, Borjan Gagoski, Divya Varadarajan, Sébastien Proulx, Martin Reuter, Jonathan R. Polimeni, Bruce Fischl, Satrajit Ghosh, and André J. W. van der Kouwe. MR software tools for real-time decision making and FOV prescription. *Proc. Intl. Soc. Magn. Reson. Med.*, 2024. [1](#)

[73] Daniel E. Worrall, Stephan J. Garbin, Daniyar Turmukhametov, and Gabriel J. Brostow. Harmonic networks: deep translation and rotation equivariance. In *IEEE Conf. Comp. Vis. and Pat. Recog.*, pages 7168–7177, 2017. [2](#)

[74] Yu Xiang, Tanner Schmidt, Venkatraman Narayanan, and Dieter Fox. PoseCNN: a convolutional neural network for 6D object pose estimation in cluttered scenes. *Robotics: Science and Systems (RSS)*, 2018. [1](#) [3](#) [4](#)

[75] Junshen Xu, Daniel Moyer, P Ellen Grant, Polina Golland, Juan Eugenio Iglesias, and Elfar Adalsteinsson. SVoRT: iterative transformer for slice-to-volume registration in fetal brain MRI. In *International Conference on Medical Image Computing and Computer-Assisted Intervention*, pages 3–13. Springer, 2022. [10](#)

[76] Junshen Xu, Daniel Moyer, Borjan Gagoski, Juan Eugenio Iglesias, P. Ellen Grant, Polina Golland, and Elfar Adalsteinsson. NeSVoR: implicit neural representation for slice-to-volume reconstruction in MRI. *IEEE Transactions on Medical Imaging*, 42(6):1707–1719, 2023. [1](#) [3](#)

[77] Ziv Yaniv and Kevin Cleary. Image-guided procedures: a review. *Computer Aided Interventions and Medical Robotics*, 3(1-63):7, 2006. [1](#)

[78] Jinfeng Zhan, Ivo D. Dinov, Junning Li, Zhonghe Zhang, Sam Hobel, Yonggang Shi, Xiangtao Lin, Alen Zamanyan, Lei Feng, Gaojun Teng, Fang Fang, Yuchun Tang, Fengchao Zang, Arthur W. Toga, and Shuwei Liu. Spatial–temporal atlas of human fetal brain development during the early second trimester. *NeuroImage*, 82:115–126, 2013. [1](#) [5](#) [6](#)

[79] Chao Zhang, Ignas Budvytis, Stephan Liwicki, and Roberto Cipolla. Rotation equivariant orientation estimation for omnidirectional localization. In *Proceedings of the Asian Conference on Computer Vision (ACCV)*, 2020. [2](#)

[80] Heng Zhao, Shenxing Wei, Dahu Shi, Wenming Tan, Zheyang Li, Ye Ren, Xing Wei, Yi Yang, and Shiliang Pu. Learning

symmetry-aware geometry correspondences for 6D object pose estimation. In *2023 IEEE/CVF International Conference on Computer Vision (ICCV)*, pages 13999–14008, 2023. [3](#), [5](#)

[81] Yi Zhou, Connally Barnes, Jingwan Lu, Jimei Yang, and Hao Li. On the continuity of rotation representations in neural networks. In *2019 IEEE/CVF Conference on Computer Vision and Pattern Recognition (CVPR)*, pages 5738–5746, 2019. [2](#)

[82] Kelly H. Zou, Simon K. Warfield, Aditya Bharatha, Clare M.C. Tempany, Michael R. Kaus, Steven J. Haker, William M. Wells, Ferenc A. Jolesz, and Ron Kikinis. Statistical validation of image segmentation quality based on a spatial overlap index1: scientific reports. *Academic Radiology*, 11(2):178–189, 2004. [7](#)

[83] Åke Björck. Solving linear least squares problems by Gram-Schmidt orthogonalization. *BIT Numerical Mathematics*, 7:1–21, 1967. [5](#)

Equivariant Symmetry-Aware Head Pose Estimation for Fetal MRI

Supplementary Material

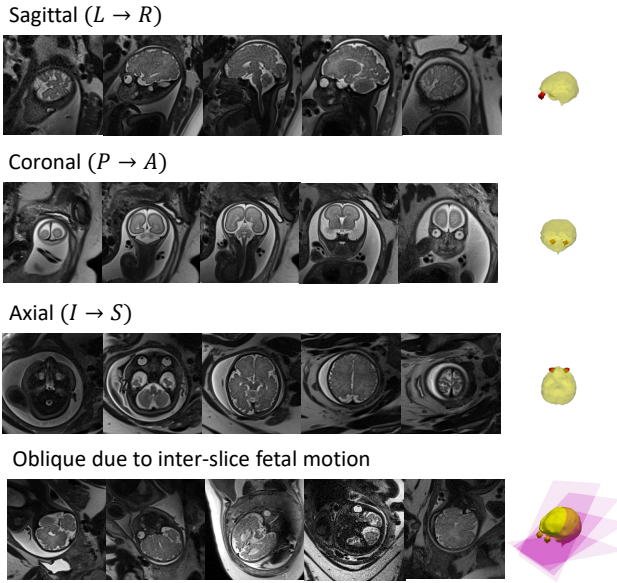


Figure 6. **Example diagnostic 2D slices.** Accurate radiological assessment of developmental abnormalities necessitates slices aligned to the sagittal (left→right), coronal (posterior→anterior), and axial (inferior→superior) anatomical directions (rows 1-3). Inter-slice fetal motion causes oblique slice orientations relative to the canonical anatomical directions (row 4). This produces slices that are challenging for the radiologist to interpret and induces coverage gaps in the acquired stack of slices.

A. Automated slice prescription

In this section, we describe our clinical application in detail.

Overview. Radiological assessment of abnormal fetal brain development relies on volumetric fetal brain MRI, which provides greater contrast and resolution than standard ultrasound examinations. Due to the high sensitivity of 3D MRI acquisitions to fetal motion, current clinical practice acquires stacks of diagnostic-quality 2D MRI slices in the three target anatomical directions (i.e., sagittal, coronal, and axial) [23]. Slices that closely align to the target anatomical orientation are critical for abnormality detection. For instance, non-oblique midline sagittal slices are necessary for detecting agenesis of the corpus callosum [22]. Furthermore, inter-slice fetal motion is often correlated with poor spatial coverage. Even small coverage gaps can substantially reduce diagnostic potential: for example, in second- and third-trimester fetuses, the proportion of the total brain volume constituted by the cerebellum ranges from only 0.03 to 0.06 [6]. Adaptive slice prescription based on the fetal head motion thus holds potential to improve the quality of

prenatal care.

Slices are T2-weighted and acquired with the half-Fourier acquisition single-shot turbo spin-echo (HASTE) MRI sequence ($1.25 \times 1.25\text{mm}$ pixels, 3mm slice thickness, $320 \times 320\text{mm}$ FOV, TR=2.5s, TE=106ms, GRAPPA R=2, Partial Fourier=5/8, 90° flip angle). Fig. 6 shows examples of slices in the target anatomical orientations, as well as *oblique* slices caused by fetal motion. To automatically prescribe the imaging plane of each slice according to the current fetal head pose, we rapidly acquire a 3D navigator volume before each slice [17]. Navigator volumes are acquired with the echo-planar imaging (EPI) sequence (4-6mm isotropic voxels, $324 \times 324 \times 120\text{mm}$ FOV, TR=29ms, TE=14ms, 5° flip angle). Low-resolution, low-energy navigator volumes are not of diagnostic quality but suffice for head pose estimation.

Automation framework. We aim to rapidly estimate the 6-DoF head pose in each navigator volume and use it to adjust the imaging plane of the next slice (Fig. 7). Formally, at the start of the sequence, we define the target imaging planes $P_1, \dots, P_K \in \text{SE}(3)$ of all K slices in the stack, relative to the canonical fetal head frame. The rotational and translational components of P_k indicate the target anatomical orientation and the relative position of the slice within the stack, respectively. Before the k th slice in the stack, we acquire a navigator volume, from which we rapidly estimate the head pose $T_k = t_k \circ R_k$ and prescribe the imaging plane of the next slice to be $\tilde{P}_k = T_k P_k$. We also translate the field-of-view (FOV) of the next navigator volume around the fetal head based on t_k . We include this step to ensure full head capture for accurate pose estimation. Because the time interval between every navigator and the next slice is 1s, we require the runtime of pose estimation to be less than 1s.

In-utero implementation [53]. We implemented our full automation framework on a GPU-enabled laptop server connected to a 3T Siemens scanner using existing software [72] (Fig. 8). We have performed preliminary evaluations of real-time navigator FOV translation on pregnant volunteers; the videos available at ramyamut.github.io/e3-pose demonstrate how the navigators are automatically shifted to follow the translational movements of the fetal head. Ongoing work is evaluating real-time slice prescription, using the full pose T_k returned by E(3)-Pose in every navigator volume.

B. E(3)-CNN implementation details

Equivariant pooling and non-linearities. E(3)-CNNs necessitate special poolings and non-linearities, since standard versions only satisfy Eq. (1) for zero-order fields. Specif-

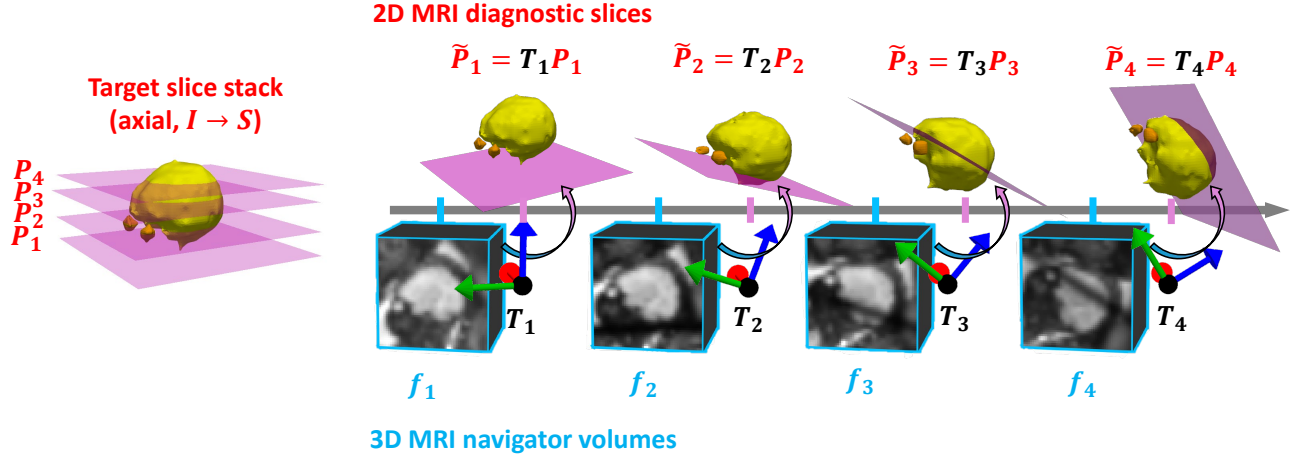


Figure 7. **Interleaved acquisition framework.** To correct for fetal head motion, we aim to automatically adjust the imaging plane P_k of every 2D slice, using the current head pose T_k . We rapidly acquire a navigator volume f_k before every slice in order to accurately estimate T_k from f_k with E(3)-Pose.

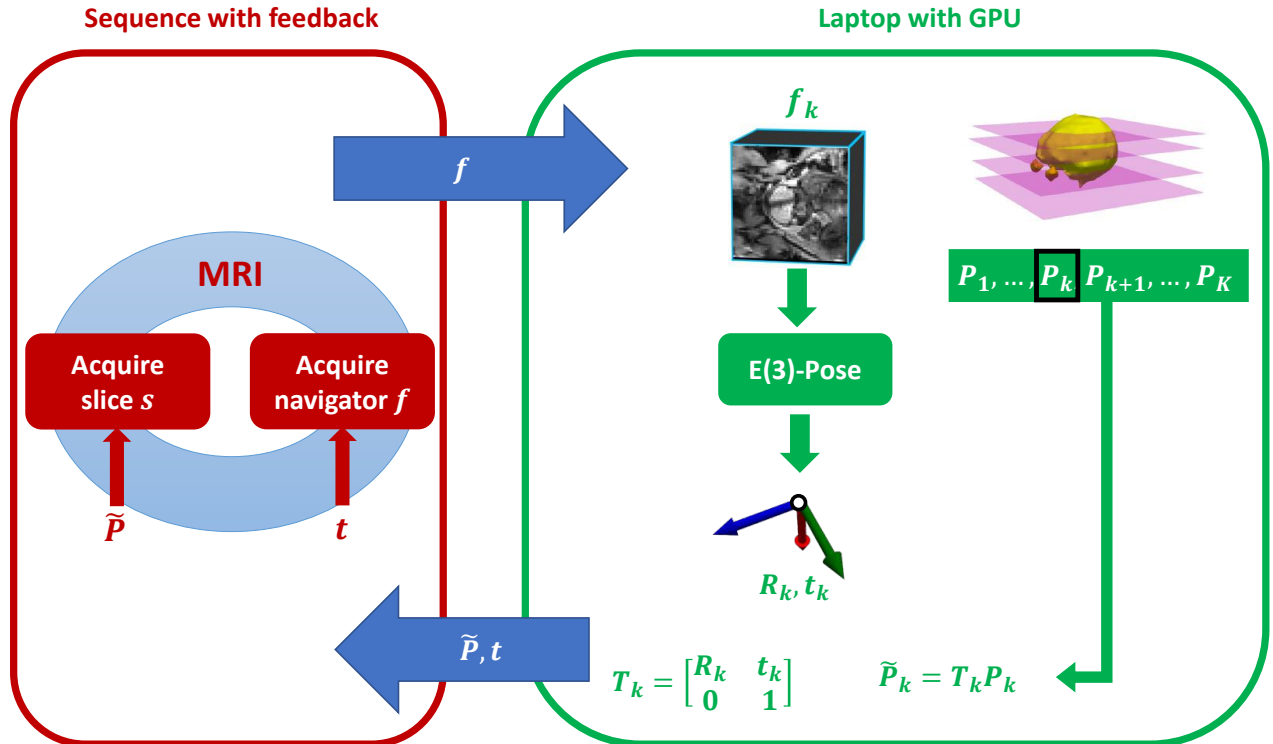


Figure 8. **Feedback loop system.** Our implementation runs on a 3T Siemens scanner, connected to a server hosted on a GPU-enabled laptop. On the server (right), E(3)-Pose separately estimates the rotation R_k and translation t_k of the fetal head pose T_k , based on the navigator volume f_k sent by the scanner (left). We apply translation t_k to center the next navigator volume FOV around the fetal head. Finally, we send the prescription parameters to the scanner for the next acquisition.

ically, higher order ($l > 0$) fields require (i) norm-based pooling, and (ii) special non-linearities learned by the network as multiplicative scalar fields: $f(x)\sigma(\kappa_{l,p,0,0} * f(x))$, where σ is the sigmoid function, and $*$ is the convolution operator [70].

Network architecture. We crop input volumes to the E(3)-CNN around the predicted brain mask to 64^3 voxels, scaled such that the brain occupies 60% of the cropped volume size. Our E(3)-CNN architecture has 4 levels, each consisting of 2 E(3)-equivariant convolutions [13, 20] with

kernel size $5 \times 5 \times 5$, followed by instance normalization and equivariant max-pooling. Following [13], the first level has 8, 4, and 2 even- and odd-parity output features of orders $l = 0, 1, 2$, respectively, and the feature count is doubled in each level. We use ReLU and tanh activations for even and odd scalar features respectively, and equivariant sigmoid activations for higher-order features. For the radial basis functions φ_m in the k^{th} level, we use $\varphi_m(r) = 8.433573 \text{sus}(x + m - 1) \text{sus}(1 - m - x)$, where sus is the soft unit step function implemented in [13] and parametrized by $m \in \{0, r/4, r/2, 3r/4, r\}$, where $r = 2^{k-2}$.

C. Segmentation network architecture

Following [63], we implement the brain segmentation function ψ with a standard 3D U-Net. Our architecture has 4 levels with 16, 32, 64, and 128 output channels, respectively, each consisting of 2 convolutional layers with kernel size $3 \times 3 \times 3$, followed by batch normalization and ELU activation [9]. Inputs are padded to 128^3 voxels. While we only use the predicted brain mask for inference, we train the U-Net to additionally segment the eyes, with the aim of enhancing the overall robustness via multi-task learning [18].

D. E(3)-CNN loss function

Below we show that in our training objective (Eq. 7), the pseudovector term $|\sin(\theta_x)|$ and the vector terms $|\sin(\theta_y/2)|$ and $|\sin(\theta_z/2)|$ are monotonically decreasing functions of the vector dot product $\hat{e}_k \cdot e_k$ and its square $(\hat{e}_k \cdot e_k)^2$, respectively.

$$\begin{aligned} |\sin(\theta_x)| &= \sqrt{1 - \cos^2(\theta_x)} \\ &= \sqrt{1 - (\hat{e}_k \cdot e_k)^2} \\ |\sin(\theta_{\{y,z\}}/2)| &= \sqrt{\frac{1 - \cos(\theta_{\{y,z\}})}{2}} \\ &= \sqrt{\frac{1 - (\hat{e}_{\{y,z\}} \cdot e_{\{y,z\}})}{2}} \end{aligned} \quad (8)$$

We note that this objective is invariant under left-right reflections, i.e., $|\sin(\theta_x)|$ remains unchanged under the transformation $e_x \rightarrow -e_x$. We observed experimentally that our choice of loss function produced more robust results than dot product, geodesic loss, and other commonly used variants (Table 2).

E. Pose annotations

Manual. We manually annotated all poses in Research-Fetal, dHCP, and Clinical-Young using ground-truth brain/eyes segmentations. We define the L→R direction as pointing from the CoM of the left eye to that of the right. We define the P→A direction as pointing from the brain CoM to the

midpoint between the eyes, rotated 25° about the L→R axis. All annotated poses were visually verified by a radiologist.

Semi-automated. To feasibly annotate poses in Navigators, a much larger dataset (1210 total volumes), we utilized algorithmically generated poses to assist with annotation. Specifically, we first algorithmically obtained P_k values for all slices, using optimization-based slice-to-volume registration [76] (recall from Appendix A that slices are prescribed according to $\tilde{P}_k = T_k P_k$). Since all \tilde{P}_k values were available to us as part of the acquisition parameters, we then computed $T_k = \tilde{P}_k P_k^{-1}$ as the GT pose for every navigator volume preceding the k^{th} slice in the stack. Lastly, we manually corrected the poses in each navigator volume.

F. Training details

Segmentation Network. We train the segmentation U-Net for 1000 epochs using Adam optimization [37] with batch size 4 and learning rate 10^{-4} . We use a weighted sum of the cross-entropy and Dice losses [50], with weights of 1 and 0.5, respectively. We re-weight both loss terms by 8, 2, and 1 for the brain, eyes, and background classes, respectively. During training and inference, we resample all input volumes to 3mm isotropic voxels before padding to 128^3 voxels.

We spatially augment training volumes with random rotations, translations, and scaling uniformly sampled from $\text{SO}(3)$, $[-30, 30]^3 \text{mm}$, and $[0.5, 1.3]$, respectively. We also simulate low resolution in 75% of training volumes, with isotropic voxel size sampled uniformly from $[3, 8] \text{mm}$. We add Gaussian noise with σ sampled uniformly from $[0, 0.03]$, random gamma correction with $\log \gamma$ sampled uniformly from $[-0.8, 0]$, and bias field artifacts. For the bias field simulation, we use existing software [55] to model the artifact as a linear combination of polynomial basis functions of order 3, with coefficients sampled uniformly from $[0, 0.5]$. For spin history artifact simulation, we sample n_{slice} uniformly from the unit sphere and σ uniformly from $[1.5, 2.3] \text{mm}$. We sample c_{slice} such that the likelihood of a point is inversely proportional to its distance from the brain boundary. In navigator volumes, when the artifact intersects regions near the boundary of the brain, there is greater uncertainty in disambiguating the brain from external uterine tissue. Thus, we provide the network with more examples of these challenging cases during training.

E(3)-CNN. We train the E(3)-CNN regressor for 2500 epochs using stochastic gradient descent with batch size 1, learning rate 10^{-2} , weight decay 3×10^{-5} , and momentum 0.99. We spatially augment training volumes with random rotations uniformly sampled from $\text{SO}(3)$. We simulate low resolution in 90% of training volumes, with isotropic voxel size sampled uniformly from $[3, 7.5] \text{mm}$. We use gamma augmentations with $\log \gamma$ sampled uniformly from

Table 3. **Performance statistics for translation estimation.** Mean \pm standard deviation for translation error (mm) are reported. Best score is in bold. * indicates statistical significance at $p < 0.05$ compared to E(3)-Pose (hierarchical permutation test for Navigators, pairwise Wilcoxon for all other datasets). We compare E(3)-Pose only to methods that estimate translation differently from E(3)-Pose. We evaluate the instance of E(3)-Pose trained on Research-Fetal since translation estimation relies only on brain segmentation. FireANTs runtime is 1.8s, prohibiting real-time deployment. See Table 6 for subject-level statistics in Navigators.

	Research-Fetal test	dHCP test	Clinical-Young	Navigators
FireANTs [35]	$2.0 \pm 2.3^*$	$0.5 \pm 1.6^*$	$0.6 \pm 0.5^*$	$4.2 \pm 3.1^*$
EquiTrack [4]	$1.3 \pm 0.9^*$	$1.1 \pm 0.7^*$	$1.6 \pm 1.6^*$	$4.4 \pm 3.2^*$
E(3)-Pose (ours)	0.9 ± 0.8	0.8 ± 0.8	0.9 ± 1.1	3.8 ± 2.8

$[-2.0, 0.1]$ and the same bias field artifact as the segmentation network. For spin history artifact simulation, we sample n_{slice} uniformly from the unit sphere and σ uniformly from $[2.3, 4.6]\text{mm}$. We sample c_{slice} uniformly from voxels in the GT brain segmentation.

G. Datasets

In this section, we provide additional information on all datasets. For Research-Fetal, Clinical-Young, and Navigators, all subjects consented to data collection, and the approval of all ethical and experimental procedures and protocols was granted by the Institutional Review Board of the Boston Children’s Hospital.

Research-Fetal. This dataset consists of whole-uterus EPI volumes in 153 pregnant volunteers (3T, Siemens, 3mm isotropic resolution, TR=2.9-4s, TE=32-47 ms, flip angle=90°). Fetus GA ranges from 18 to 38 weeks, with mean GA 29.0 ± 5.0 weeks. The average FOV size is $300 \times 300 \times 156\text{mm}$.

dHCP. This dataset consists of fetal brain EPI volumes in 245 pregnant volunteers (3T, Philips Achieva, 2.2mm isotropic resolution, TR=2.2s, TE=60ms, flip angle=90°) [36]. Fetus GA ranges from 20 to 38 weeks, with mean GA 28.9 ± 3.8 weeks. The average FOV size is $143 \times 151 \times 108\text{mm}$. Volumes are cropped around the fetal head and are not whole-uterus volumes. Our manually annotated brain/eyes segmentations and poses for the dHCP dataset are publicly available on the project website for full transparency and future use.

Clinical-Young. This dataset consists of routine clinical whole-uterus EPI volumes in 60 pregnant patients (3T, Siemens, 1.76-3.5mm voxels, TR=2.2-5s, TE=37ms, flip angle=90°). There are 10 subjects for each GA in the range of 18 to 23 weeks. The average FOV size is $301 \times 301 \times 129\text{mm}$. Additionally, we note that while Clinical-Young is not representative of our target application of automated slice prescription, it is representative of routine clinical data acquired for retrospective head pose tracking, which promises to enable early disease detection. Specifically, there is well-supported evidence that fetal motion patterns correlate with neurodevelopmental disorders and

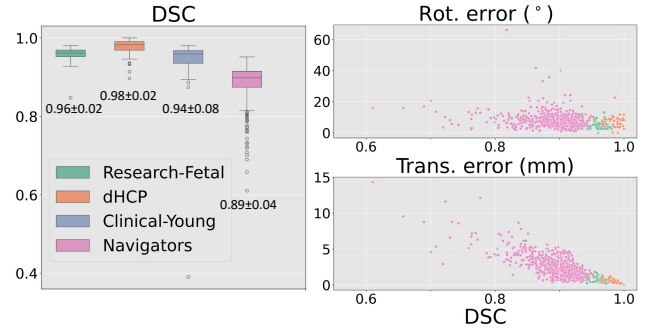


Figure 9. **Segmentation study.** Our segmentation network (trained on Research-Fetal) predicts accurate brain masks on all datasets, including challenging, out-of-distribution navigator volumes (*left*). Rotation estimation with the E(3)-CNN remains robust to larger segmentation errors observed in Navigators (*top right*), while translation estimation displays sensitivity to error (*bottom right*).

intrauterine complications [1, 46].

Navigators. This dataset consists of 47 stacks of 2D HASTE slices (3T, Siemens, TR=3-3.5s, TE=100ms, $1.25 \times 1.25 \times 3\text{mm}$, FA=90°) interleaved with 3D EPI navigator volumes (3T, Siemens, TR=25-46ms, 4-6mm, TE=12-22ms, flip angle=5°) in 9 pregnant volunteers. Fetus GA ranges from 26 to 36 weeks, with mean GA 30.6 ± 2.9 weeks. The average FOV size is $327 \times 327 \times 125\text{mm}$. This dataset is most representative of automated slice prescription, and navigator volumes contain real spin history artifacts.

H. Baseline methods

We describe our implementations of the baseline methods and the modifications we make in order to optimize performance of baseline algorithms for our experiments. All methods that rely on network training were trained on a Nvidia RTX 6000 Ada GPU with batch size of either 4 or 5, unless otherwise stated.

FireANTs [35]. We initialize pose estimates with moments-of-inertia matching, followed by multi-resolution adaptive gradient optimization with learning rate 3×10^{-4} at downampling factors of 4, 2, and 1 with 200, 100, and 50 iterations respectively. We find that the initialization step helps boost performance particularly in the case of large rotational mis-

Table 4. **Subject-level baseline comparisons for rotation error (°) in Navigators.** Mean \pm 95% confidence interval statistics are displayed. Subjects are denoted by gestational age (GA, weeks). Best score is in bold. * indicates statistical significance compared to E(3)-Pose ($p < 0.05$, permutation test). See Table 1 for additional details.

Subject (GA)	S1 (28w)	S2 (28w)	S3 (32w)	S4 (34w)	S5 (36w)	S6 (28w)	S7 (26w)	S8 (31w)	S9 (28w)
FireANTs [35]	65.7 \pm 8.2*	62.8 \pm 8.6*	49.4 \pm 12.9*	10.0 \pm 1.2*	53.5 \pm 8.1*	75.8 \pm 14.3*	28.7 \pm 6.4*	8.6 \pm 1.7	24.0 \pm 8.6*
Fetal-Align [32]	13.2 \pm 4.1*	90.3 \pm 5.3*	52.3 \pm 10.5*	35.7 \pm 8.6*	115.3 \pm 8.4*	62.3 \pm 11.2*	21.3 \pm 4.2*	10.7 \pm 3.9	29.4 \pm 9.3*
Trained on Research-Fetal									
EquiTrack [4]	40.1 \pm 6.0*	63.9 \pm 6.6*	37.7 \pm 8.2*	45.5 \pm 9.8*	45.3 \pm 6.6*	97.5 \pm 12.6*	24.2 \pm 4.3*	28.5 \pm 8.2*	21.3 \pm 8.5*
3DPose-Net [59]	54.7 \pm 6.0*	113.4 \pm 5.6*	98.6 \pm 8.7*	56.4 \pm 6.7*	30.2 \pm 2.8*	101.5 \pm 9.3*	65.9 \pm 7.6*	35.2 \pm 6.1*	37.8 \pm 4.5*
6DRep [15]	23.1 \pm 2.5*	95.0 \pm 7.0*	24.4 \pm 3.9*	36.2 \pm 7.8*	11.7 \pm 1.8	52.6 \pm 9.7*	46.3 \pm 8.7*	18.5 \pm 5.1*	19.2 \pm 1.6*
RbR [24]	20.7 \pm 2.9*	43.3 \pm 3.8*	20.6 \pm 3.8*	10.7 \pm 1.2*	10.4 \pm 1.2	51.8 \pm 10.1*	26.0 \pm 3.0*	11.0 \pm 0.9*	9.3 \pm 0.8*
E(3)-Pose (ours)	6.4 \pm 0.5	13.6 \pm 1.5	10.6 \pm 3.4	6.6 \pm 0.6	10.7 \pm 0.8	13.4 \pm 1.9	9.2 \pm 0.8	8.4 \pm 1.0	7.4 \pm 0.6
Trained on dHCP									
EquiTrack [4]	32.9 \pm 5.8*	66.3 \pm 6.8*	65.2 \pm 12.2*	75.5 \pm 9.9*	76.7 \pm 8.5*	109.4 \pm 10.4*	18.8 \pm 3.8	68.5 \pm 13.4*	36.4 \pm 10.9
3DPose-Net [59]	138.8 \pm 3.1*	100.2 \pm 3.5*	139.8 \pm 4.7*	115.7 \pm 4.7*	16.8 \pm 1.7*	69.4 \pm 4.7*	79.6 \pm 3.0*	54.1 \pm 3.7*	102.9 \pm 2.9*
6DRep [15]	55.2 \pm 4.2*	153.1 \pm 4.2*	72.6 \pm 2.9*	82.2 \pm 12.7*	17.0 \pm 1.1*	38.6 \pm 3.3*	137.8 \pm 3.6*	79.5 \pm 4.2*	115.4 \pm 7.7*
RbR [24]	45.3 \pm 3.2*	121.0 \pm 4.1*	100.8 \pm 5.4*	41.1 \pm 6.4*	23.1 \pm 4.1*	118.6 \pm 8.0*	145.6 \pm 4.5*	86.3 \pm 8.0*	37.1 \pm 4.9*
E(3)-Pose (ours)	12.7 \pm 1.6	24.4 \pm 2.6	14.4 \pm 3.3	6.5 \pm 0.5	9.2 \pm 0.9	14.9 \pm 1.7	16.9 \pm 2.2	7.0 \pm 0.8	14.2 \pm 1.7

Table 5. **Subject-level baseline comparisons for average absolute distance (AAD, mm) in Navigators.** Mean \pm 95% confidence interval statistics are displayed. See Table 4 for description.

Subject (GA)	S1 (28w)	S2 (28w)	S3 (32w)	S4 (34w)	S5 (36w)	S6 (28w)	S7 (26w)	S8 (31w)	S9 (28w)
FireANTs [35]	24.4 \pm 2.5*	22.5 \pm 2.6*	22.5 \pm 4.7*	6.2 \pm 0.7*	27.5 \pm 3.8*	33.1 \pm 4.8*	12.1 \pm 2.1*	5.8 \pm 0.9	11.2 \pm 3.0*
Fetal-Align [32]	7.4 \pm 1.4*	36.2 \pm 2.0*	27.4 \pm 4.8*	18.8 \pm 3.8*	49.5 \pm 3.3*	29.0 \pm 4.5*	9.5 \pm 1.6*	6.0 \pm 1.6	13.4 \pm 3.8*
Trained on Research-Fetal									
EquiTrack [4]	17.5 \pm 2.1*	25.7 \pm 2.2*	19.9 \pm 3.2*	21.9 \pm 3.8*	23.7 \pm 2.8*	41.4 \pm 4.1*	11.4 \pm 1.5*	13.0 \pm 2.9*	9.3 \pm 2.9*
3DPose-Net [59]	23.1 \pm 2.1*	42.1 \pm 1.6*	43.2 \pm 2.6*	29.7 \pm 2.6*	17.5 \pm 1.4*	43.1 \pm 2.7*	24.3 \pm 2.3*	16.3 \pm 2.2*	17.2 \pm 1.9*
6DRep [15]	11.4 \pm 1.1*	36.5 \pm 2.2*	14.2 \pm 2.0*	18.7 \pm 3.2*	7.9 \pm 0.9	25.9 \pm 3.5*	16.5 \pm 2.5*	9.0 \pm 2.0*	9.1 \pm 0.7*
RbR [24]	10.4 \pm 1.1*	19.4 \pm 1.4*	12.2 \pm 1.8*	7.4 \pm 0.6*	7.3 \pm 0.7	25.8 \pm 4.1*	11.0 \pm 1.1*	6.3 \pm 0.5*	5.0 \pm 0.4*
E(3)-Pose (ours)	5.0 \pm 0.3	7.6 \pm 0.7	7.5 \pm 1.7	5.5 \pm 0.2	7.4 \pm 0.5	10.1 \pm 1.2	4.8 \pm 0.3	5.1 \pm 0.5	4.1 \pm 0.3
Trained on dHCP									
EquiTrack [4]	14.8 \pm 2.2*	26.1 \pm 2.3*	29.8 \pm 4.7*	36.2 \pm 4.1*	36.8 \pm 3.4*	45.9 \pm 2.7*	8.3 \pm 1.3	25.2 \pm 4.4*	14.7 \pm 3.7
3DPose-Net [59]	49.5 \pm 0.6*	38.2 \pm 1.1*	60.1 \pm 1.0*	54.0 \pm 1.5*	10.5 \pm 0.9*	33.8 \pm 1.8*	31.2 \pm 1.0*	26.5 \pm 1.5*	40.9 \pm 0.9*
6DRep [15]	23.9 \pm 1.6*	49.8 \pm 1.0*	36.0 \pm 1.3*	35.2 \pm 4.7*	10.8 \pm 10.6*	20.4 \pm 1.5*	44.5 \pm 0.7*	36.8 \pm 1.7*	45.0 \pm 2.0*
RbR [24]	20.4 \pm 1.2*	43.5 \pm 0.9*	48.3 \pm 1.8*	21.7 \pm 2.8*	13.2 \pm 1.8*	48.5 \pm 2.4*	45.4 \pm 0.8*	34.7 \pm 2.7*	17.1 \pm 1.8*
E(3)-Pose (ours)	7.3 \pm 0.7	11.9 \pm 1.0	9.2 \pm 1.6	5.4 \pm 0.3	6.7 \pm 0.6	10.6 \pm 1.1	7.9 \pm 0.9	4.5 \pm 0.4	7.2 \pm 0.8

Table 6. **Subject-level baseline comparisons for translation error (mm) in Navigators.** Mean \pm 95% confidence interval statistics are displayed. See Table 4 for description.

Subject (GA)	S1 (28w)	S2 (28w)	S3 (32w)	S4 (34w)	S5 (36w)	S6 (28w)	S7 (26w)	S8 (31w)	S9 (28w)
FireANTs [35]	3.6 \pm 0.3*	4.6 \pm 0.4*	5.8 \pm 1.1*	2.7 \pm 0.3*	4.6 \pm 0.4*	8.1 \pm 1.0*	3.0 \pm 0.2*	3.4 \pm 0.3*	3.5 \pm 0.4*
EquiTrack [4]	4.0 \pm 0.3	5.6 \pm 0.5*	5.1 \pm 1.0	3.7 \pm 0.5	3.9 \pm 0.4*	7.5 \pm 1.0	4.5 \pm 0.3*	3.1 \pm 0.3*	2.1 \pm 0.3*
E(3)-Pose (ours)	4.0 \pm 0.3	4.2 \pm 0.4	5.0 \pm 1.0	3.9 \pm 0.2	3.6 \pm 0.4	7.4 \pm 0.9	2.7 \pm 0.2	2.6 \pm 0.2	2.0 \pm 0.3

Table 7. **Subject-level ablation study for rotation error (°) in Navigators.** Mean \pm 95% confidence interval statistics are displayed. See Table 4 for description.

Subject (GA)	S1 (28w)	S2 (28w)	S3 (32w)	S4 (34w)	S5 (36w)	S6 (28w)	S7 (26w)	S8 (31w)	S9 (28w)
Trained on Research-Fetal									
E(3)-Pose (ours)	6.4 \pm 0.5	13.6 \pm 1.5	10.6 \pm 3.4	6.6 \pm 0.6	10.7 \pm 0.8	13.4 \pm 1.9	9.2 \pm 0.8	8.4 \pm 1.0	7.4 \pm 0.6
Standard CNN	10.8 \pm 0.4*	32.4 \pm 4.0*	19.8 \pm 4.1*	12.7 \pm 2.3*	10.2 \pm 0.9	22.5 \pm 4.3*	29.0 \pm 3.7*	11.7 \pm 1.7*	7.5 \pm 0.6
no pseudovector	9.4 \pm 0.9*	15.8 \pm 2.4*	11.2 \pm 3.2	5.8 \pm 0.5*	12.6 \pm 1.0*	18.0 \pm 4.0*	8.7 \pm 1.0	6.2 \pm 0.6*	8.6 \pm 0.6*
$h(R) = e_y \oplus e_z$	7.5 \pm 0.6*	19.7 \pm 2.9*	11.0 \pm 3.6*	6.5 \pm 0.8	9.6 \pm 0.7*	20.8 \pm 2.5*	14.0 \pm 2.2*	9.7 \pm 0.8	7.3 \pm 0.7
$\mathcal{L}_\phi = \sum_{k \in \{x, y, z\}} \sin(\theta_k/2) $	7.9 \pm 0.5*	19.2 \pm 2.2*	12.8 \pm 3.6*	7.4 \pm 0.9	11.1 \pm 0.9	19.8 \pm 3.6*	10.9 \pm 1.3*	10.5 \pm 0.8*	8.7 \pm 0.6*
geodesic loss	7.2 \pm 0.5*	25.8 \pm 4.6*	12.6 \pm 3.4*	6.4 \pm 0.5	12.9 \pm 1.6*	23.1 \pm 5.9*	14.1 \pm 3.7*	6.2 \pm 0.7*	8.7 \pm 1.1*
no artifact augmentation	11.6 \pm 1.5*	22.7 \pm 3.1*	11.8 \pm 3.6	15.5 \pm 2.5*	13.0 \pm 1.0*	35.8 \pm 7.0*	15.5 \pm 3.2*	11.9 \pm 2.2*	12.3 \pm 4.2*
Trained on dHCP									
E(3)-Pose (ours)	12.7 \pm 1.6	24.4 \pm 2.6	14.4 \pm 3.3	6.5 \pm 0.5	9.2 \pm 0.9	14.9 \pm 1.7	16.9 \pm 2.2	7.0 \pm 0.8	14.2 \pm 1.7
Standard CNN	93.9 \pm 6.9*	108.0 \pm 3.7*	147.0 \pm 4.7*	28.4 \pm 3.9*	11.7 \pm 1.0*	105.4 \pm 2.9*	111.8 \pm 6.0*	80.6 \pm 12.1*	86.3 \pm 4.1*
no pseudovector	13.1 \pm 1.9	45.3 \pm 5.3*	21.9 \pm 4.4*	8.9 \pm 1.1*	9.4 \pm 0.9	32.7 \pm 9.6*	21.9 \pm 3.2*	5.9 \pm 0.7*	23.7 \pm 3.6*
$h(R) = e_y \oplus e_z$	11.2 \pm 1.2	43.7 \pm 6.1*	15.0 \pm 5.0	8.8 \pm 0.9*	11.4 \pm 1.5*	38.1 \pm 8.7*	66.1 \pm 8.3*	10.7 \pm 3.1*	25.3 \pm 5.0*
$\mathcal{L}_\phi = \sum_{k \in \{x, y, z\}} \sin(\theta_k/2) $	9.4 \pm 0.9*	28.0 \pm 4.3	16.7 \pm 5.2	7.7 \pm 0.7*	8.7 \pm 0.8	29.3 \pm 8.4*	42.5 \pm 7.7*	9.5 \pm 3.1	15.9 \pm 1.5
geodesic loss	18.9 \pm 4.8*	47.8 \pm 7.1*	47.5 \pm 14.5*	11.1 \pm 0.8*	13.8 \pm 1.1*	35.5 \pm 8.8*	28.6 \pm 6.7*	32.3 \pm 11.1*	22.5 \pm 7.1*
no artifact augmentation	40.9 \pm 6.7*	47.6 \pm 5.8*	34.3 \pm 8.3*	22.5 \pm 6.1*	16.5 \pm 2.2*	55.0 \pm 9.7*	26.9 \pm 5.0*	19.5 \pm 4.4*	28.2 \pm 4.7*

Table 8. **Subject-level ablation study for average absolute distance (AAD, mm) in Navigators.** Mean \pm 95% confidence interval statistics are displayed. See Table 4 for description.

Subject (GA)	S1 (28w)	S2 (28w)	S3 (32w)	S4 (34w)	S5 (36w)	S6 (28w)	S7 (26w)	S8 (31w)	S9 (28w)
Trained on Research-Fetal									
E(3)-Pose (ours)	5.0 \pm 0.3	7.6 \pm 0.7	7.5 \pm 1.7	5.5 \pm 0.2	7.4 \pm 0.5	10.1 \pm 1.2	4.8 \pm 0.3	5.1 \pm 0.5	4.1 \pm 0.3
Standard CNN	6.3 \pm 0.3*	14.9 \pm 1.5*	12.0 \pm 1.9*	8.9 \pm 1.1*	7.6 \pm 0.5	14.0 \pm 1.9*	11.9 \pm 1.2*	6.5 \pm 0.8*	4.3 \pm 0.4
no pseudovector	5.9 \pm 0.4*	8.7 \pm 0.9*	8.5 \pm 1.5	5.3 \pm 0.2	8.7 \pm 0.6*	11.9 \pm 1.8*	4.7 \pm 0.4	4.1 \pm 0.3*	4.8 \pm 0.3*
$h(R) = e_y \oplus e_z$	5.5 \pm 0.3*	10.1 \pm 1.1*	8.2 \pm 1.6	5.7 \pm 0.4	7.3 \pm 0.5	13.2 \pm 1.3*	6.5 \pm 0.7*	5.5 \pm 0.4	4.1 \pm 0.3
$\mathcal{L}_\phi = \sum_{k \in \{x, y, z\}} \sin(\theta_k/2) $	5.4 \pm 0.3*	9.7 \pm 0.9*	8.4 \pm 1.7*	5.8 \pm 0.5	7.6 \pm 0.6	12.7 \pm 1.6*	5.5 \pm 0.5*	5.9 \pm 0.4*	4.8 \pm 0.3*
geodesic loss	5.1 \pm 0.3	11.7 \pm 1.6*	8.4 \pm 1.6*	5.3 \pm 0.3	8.5 \pm 10.8*	14.1 \pm 2.4*	6.4 \pm 1.2*	4.1 \pm 0.4*	4.7 \pm 0.5*
no artifact augmentation	6.8 \pm 0.6*	11.2 \pm 1.2*	8.7 \pm 1.6*	9.5 \pm 21.1*	8.9 \pm 0.6*	18.9 \pm 2.6*	7.1 \pm 1.1*	6.6 \pm 1.0*	6.1 \pm 1.6*
Trained on dHCP									
E(3)-Pose (ours)	7.3 \pm 0.7	11.9 \pm 1.0	9.2 \pm 1.6	5.4 \pm 0.3	6.7 \pm 0.6	10.6 \pm 1.1	7.9 \pm 0.9	4.5 \pm 0.4	7.2 \pm 0.8
Standard CNN	35.0 \pm 2.0*	39.4 \pm 0.8*	57.0 \pm 0.7*	16.1 \pm 1.9*	8.0 \pm 0.6*	47.1 \pm 1.1*	38.6 \pm 1.2*	32.0 \pm 4.0*	39.3 \pm 1.6*
no pseudovector	7.3 \pm 0.8	19.9 \pm 2.0*	13.0 \pm 2.0*	6.5 \pm 0.6*	6.8 \pm 0.6	16.9 \pm 3.2*	9.6 \pm 1.2*	4.0 \pm 0.3*	11.5 \pm 1.5*
$h(R) = e_y \oplus e_z$	6.8 \pm 0.5	18.2 \pm 2.0*	9.4 \pm 2.1	6.4 \pm 0.4*	7.9 \pm 0.9*	20.3 \pm 3.5*	24.1 \pm 2.5*	6.0 \pm 1.1*	12.2 \pm 2.1*
$\mathcal{L}_\phi = \sum_{k \in \{x, y, z\}} \sin(\theta_k/2) $	6.1 \pm 0.4*	12.7 \pm 1.5	10.1 \pm 2.3	6.0 \pm 0.3*	6.4 \pm 0.5	16.0 \pm 3.1*	16.1 \pm 2.4*	5.5 \pm 1.1*	8.2 \pm 0.7*
geodesic loss	9.2 \pm 1.5*	19.0 \pm 2.3*	20.7 \pm 5.3*	7.2 \pm 0.4*	8.9 \pm 0.6*	18.7 \pm 3.2*	11.0 \pm 1.9*	12.4 \pm 3.4*	10.2 \pm 2.4*
no artifact augmentation	17.4 \pm 2.3*	20.2 \pm 2.0*	18.3 \pm 3.6*	12.5 \pm 2.5*	10.5 \pm 1.1*	26.5 \pm 3.8*	11.3 \pm 1.8*	9.7 \pm 1.8*	13.6 \pm 2.0*

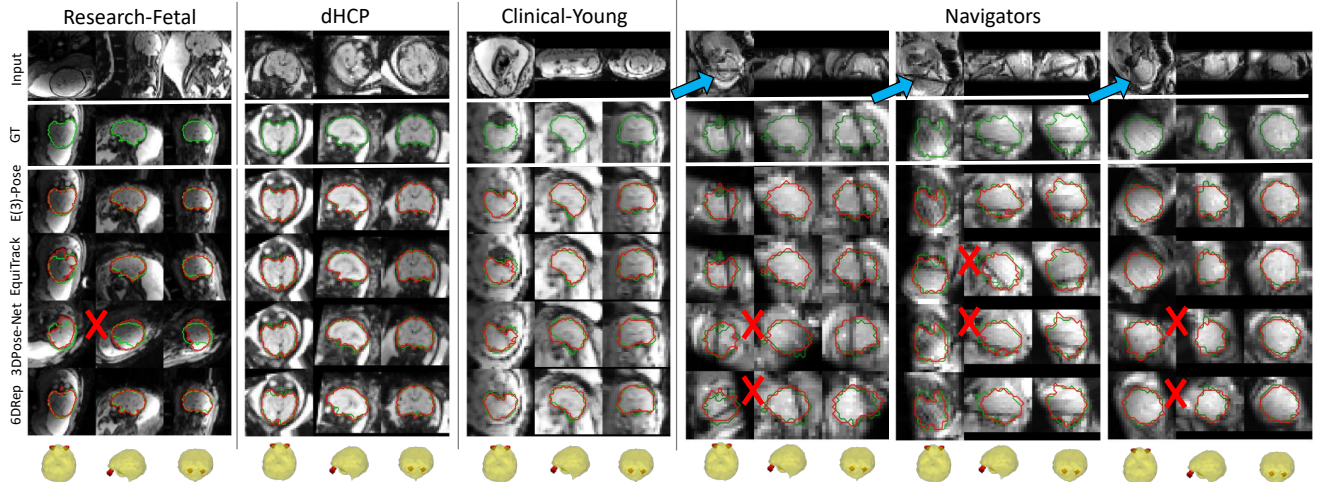


Figure 10. **Example results comparing E(3)-Pose to EquiTrack, 3DPose-Net, and 6DRep, trained on Research-Fetal.** See Fig. 3 in the main paper for descriptions.

alignment between the input and template volumes.

EquiTrack [4]. This method first uses a “denoiser” CNN to remove intensity differences between input and template volumes, followed by a $SE(3)$ -equivariant network that learns matching landmarks for rigid registration. Here, we slightly modify EquiTrack to guarantee fair comparison with our method on Navigators. First, to account for spin history artifacts, we train the denoiser network using our data augmentation strategy, which simulates these artifacts. Second, to further boost robustness to disruptive intensity perturbations (e.g., spin history artifacts), we use RANSAC [16] to compute the optimal rigid transform from matching landmarks. We train the denoiser and equivariant network for 550 and 2500 epochs with batch sizes of 4 and 1, respectively. Although we observed no statistically significant differences in performance statistics in Research-Fetal and dHCP, our

modifications led to significant improvements of 5.1° and 10.2° in rotation error in Clinical-Young and Navigators, respectively.

Fetal-Align [32]. The original implementation uses standard image processing techniques (i.e., detection of maximally stable extremal regions [48]) conditioned on GA, rather than deep learning, to estimate brain and eye masks in fetal brain volumes. We find that this approach to segmentation becomes unstable when applied to our data. For fair evaluation of landmark-based pose estimation, we use the brain and eye masks predicted by our segmentation U-Net trained on simulated spin history artifacts. When eye detection fails (a common occurrence when the artifact obstructs the eyes in navigator volumes), we return the identity transformation as an estimate of rotation. Our substitution of hand-crafted image features for deep learning-based segmentation pro-

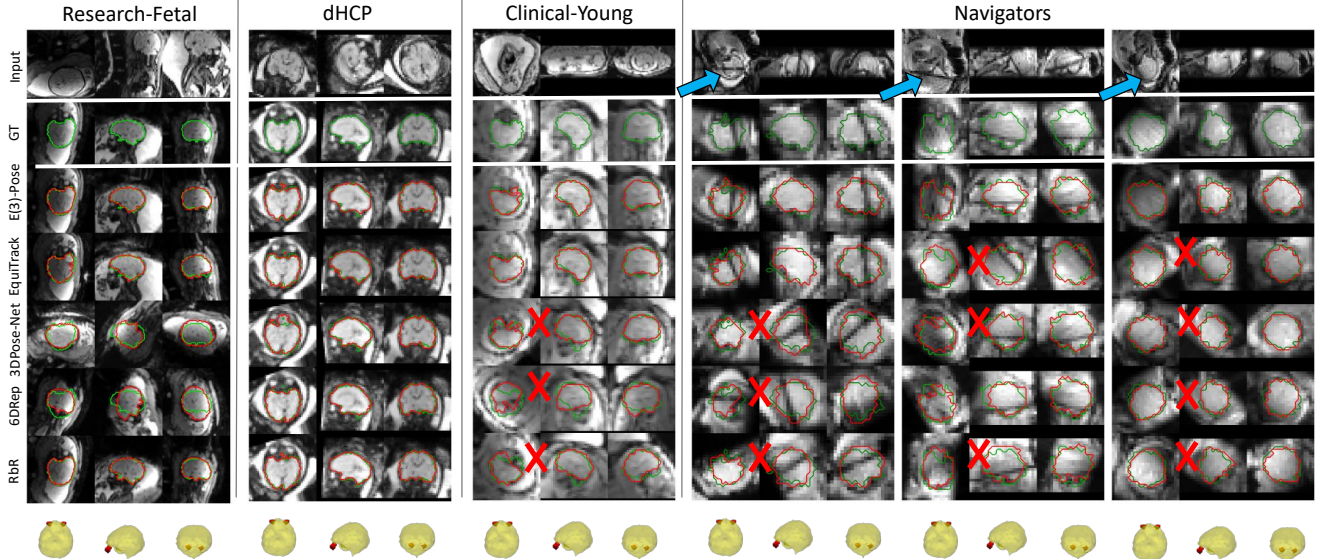


Figure 11. **Example results for methods trained on dHCP.** We omit FireANTS and Fetal-Align since these methods are not trained on dHCP. See Fig. 3 in the main paper for descriptions.

duced improvements in rotation error of 68.9° and 22.4° in Research-Fetal and dHCP, respectively; the improvements in clinical volumes were larger.

3DPose-Net [59]. For our training experiments on Research-Fetal, we use the same augmentations as that of E(3)-Pose. For our training experiments on dHCP, we tune the data augmentation parameters such that $\log \gamma$ is sampled uniformly from $[-3, -1]$ and voxel size is sampled uniformly from $[3, 9]\text{mm}$. We train the network for 8000 epochs.

6DRep [15]. We use the same training augmentations as 3DPose-Net and train the network for 7500 epochs.

RbR [24]. We find that this method provides more stable and accurate pose estimates on fetal brain volumes that are preprocessed with the same steps as our E(3)-CNN, i.e., inputs that are center-of-mass aligned and scaled based on the size of the brain. Since center-of-mass alignment of input volumes eliminates the need for translation estimation, we keep the translation estimation of E(3)-Pose and predict only rotation with the output of RbR. We use the same training augmentations as 3DPose-Net. We use Adam optimization with learning rate 10^{-4} to train the network for 4000 epochs.

I. Additional results

Evaluation of translation estimation. We separately evaluate the accuracy of translation estimation with our segmentation network by providing the translation error $\|\hat{t} - t\|_2$. We compare E(3)-Pose to baseline methods that estimate translation differently from E(3)-Pose, i.e., FireANTS and EquiTrack. Tables 3 and 6 show that E(3)-Pose outperforms

both FireANTS and EquiTrack in Navigators. The presence of spin history artifacts breaks the assumption of similarity of the intensity distributions between the input and template volumes. Compared to the template-based alignment strategy, template-free pose regression improves robustness to highly disruptive artifacts.

Evaluation of segmentation. We quantify the performance of our segmentation network by measuring the overlap between predicted and ground-truth brain masks with the Dice-Sorensen Coefficient (DSC) [82]. Our segmentation network yields mean DSC of 0.96, 0.98, 0.94, and 0.89 on Research-Fetal, dHCP, Clinical-Young, and Navigators, respectively (Fig. 9, left). While brain segmentation is robust across datasets, larger errors tend to occur in Navigators, which pose a challenging domain gap from the training data. We further observe that rotation estimation using our E(3)-CNN remains robust to segmentation errors, particularly larger errors in Navigators (Fig. 9, top right). This result highlights the advantages of a neural architecture constructed with strong inductive biases, coupled with a cropping margin large enough for the input volume to capture relevant anatomy regardless of segmentation errors. However, translation estimation is sensitive to segmentation error, since it is directly computed from the predicted mask (Fig. 9, bottom right).

Subject-level analysis in Navigators. To provide further insight, we aggregate performance statistics for each subject in Navigators. Tables 4–6 show that E(3)-Pose consistently outperforms the baselines across subjects and training datasets. Tables 7 and 8 show that regardless of the training data,

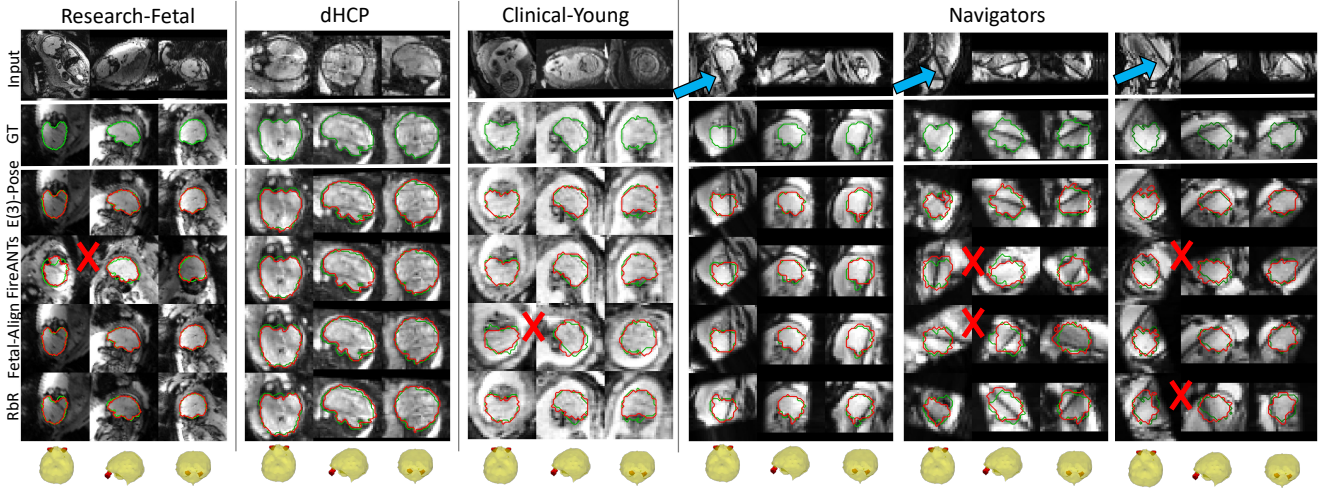


Figure 12. Additional example results for methods trained on Research-Fetal. See Fig. 3 in the main paper for descriptions.

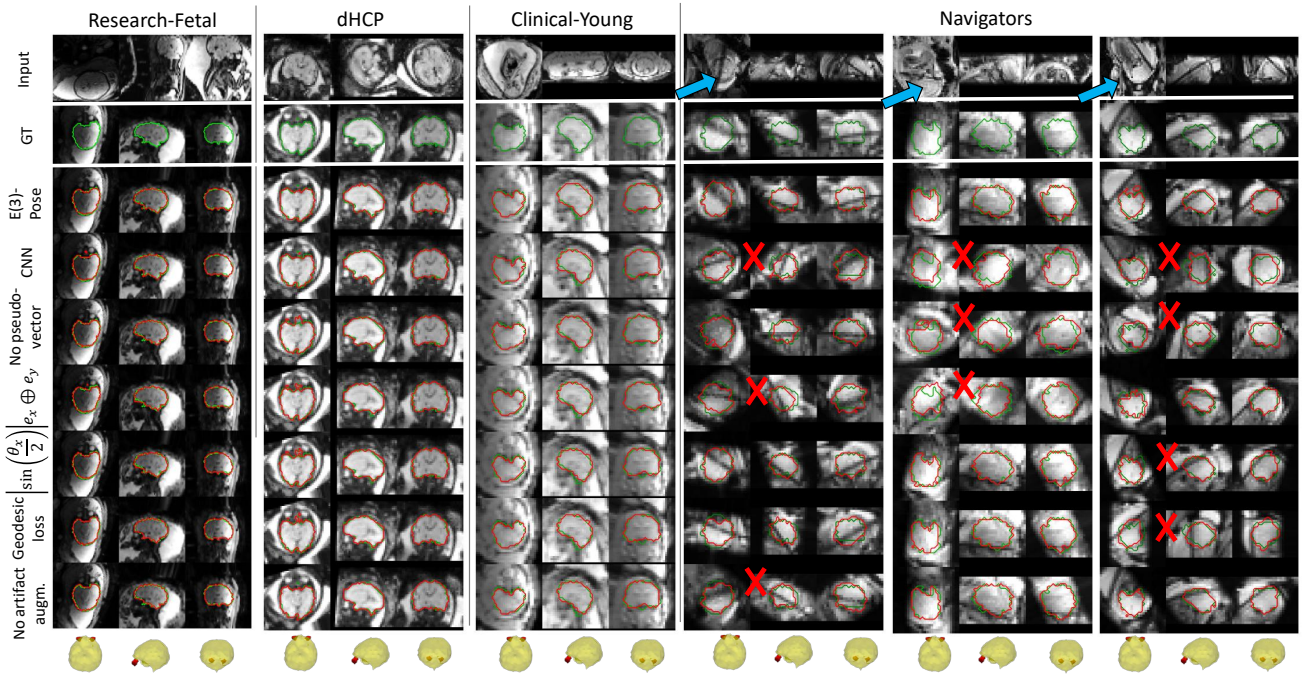


Figure 13. Example results for ablations trained on Research-Fetal. See Fig. 3 in the main paper for descriptions.

E(3)-Pose ranks first, compared to all ablations, in the greatest number of subjects. Importantly, we highlight that for several subjects (S2 and S6), E(3)-Pose significantly outperforms all ablations. From visual inspection, we observe that these cases exhibit higher inherent pose ambiguity.

Additional examples. In this section, we provide additional example alignments. Fig. 10 displays the same volumes aligned by the baseline methods that were omitted from Fig. 3 in the main paper, i.e., EquiTrack, 3DPose-Net, and 6DRep. Fig. 11 displays the same set of volumes aligned by

all methods trained on dHCP. Fig. 12 replicates Fig. 3 for a different set of test volumes in each dataset. Fig. 13 provides example alignments for E(3)-Pose and all ablations.

J. Sensitivity study

Intensity perturbations. To understand performance gaps between Research-Fetal and Navigators, we assess robustness to simulated larger voxel size and spin history artifacts in test volumes from Research-Fetal (Fig. 14). E(3)-Pose remains much more consistent than all five tested baseline

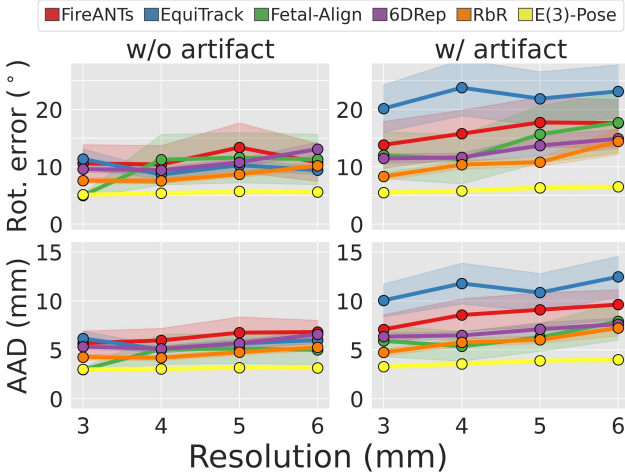


Figure 14. **Sensitivity to intensity perturbations.** We evaluate all well-performing methods trained on Research-Fetal on augmented test volumes in Research-Fetal. E(3)-Pose remains robust to progressively larger voxel sizes (left), even when simulating additional spin history artifacts (right).

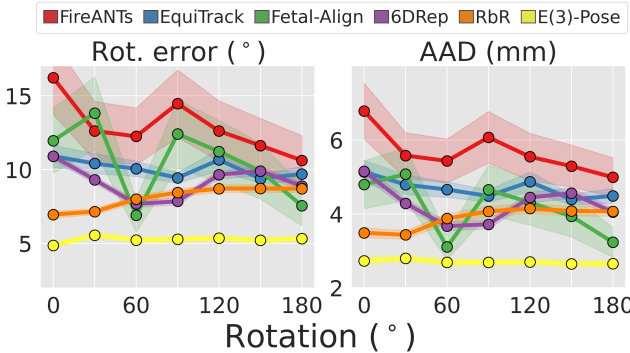


Figure 15. **Sensitivity to spatial perturbations.** We evaluate all well-performing methods trained on Research-Fetal on rotated test volumes in Research-Fetal. E(3)-Pose demonstrates stable pose estimates across a wide range of input poses.

algorithms, which become increasingly error-prone as the severity of the perturbation increases. Particularly, E(3)-Pose exhibits the smallest increase in both error metrics from the original 3mm volumes to the 6mm volumes with simulated spin history artifacts. This is particularly the case for template-dependent methods, which are highly sensitive to the presence of disruptive artifacts. Furthermore, while E(3)-Pose, 6DRep and RbR are trained on volumes augmented with these intensity transformations, E(3)-Pose significantly outperforms 6DRep and RbR on 6mm volumes with artifacts ($p < 0.05$, pairwise Wilcoxon). This result demonstrates that E(3)-CNNs display more effective generalization than standard CNNs.

Spatial perturbations. To evaluate robustness of the method across input poses, we use test volumes from Research-Fetal

to simulate a wide range of rotational misalignments of the canonical object frame relative to the input volume. E(3)-Pose displays the most stable consistency across rotational misalignments (Fig. 15). This result underscores the value of modeling rotation equivariance in pose estimation.

K. Ablation study

Alternative loss functions. In this section, we explain why the selected loss functions for our ablation experiments are not invariant under G_{symm} . Regarding the loss function where we replace the term $|\sin(\theta_x)|$ with $|\sin(\theta_x/2)|$, Appendix D shows that $|\sin(\theta_x/2)|$ is monotonically related to $\hat{e}_x \cdot e_x$, which may change in value under the transformation $e_x \rightarrow -e_x$, i.e., left-right reflection. Regarding the geodesic loss, which measures the geodesic distance $d_{\text{geo}}(\hat{R}, R)$ between the predicted and ground-truth rotations $\hat{R}, R \in \text{SO}(3)$, it requires converting the network outputs $(\hat{e}_x, \hat{e}_y, \hat{e}_z)$ to a proper rotation \hat{R} via SVD. Although this process is approximately invariant under left-right reflections when $(\hat{e}_x, \hat{e}_y, \hat{e}_z) \approx (e_x, e_y, e_z)$, this condition is not guaranteed, especially at the start of training.

Results on research data. Table 9 reports the performance statistics on research data for the ablations corresponding to Table 2 in the main paper. For most experiments, there is no significant difference in performance metrics between E(3)-Pose and ablations. These results suggest that modeling inherent symmetries by construction yields competitive accuracy but does not improve performance on in-distribution, high-SNR volumes. Specifically, methods that do not explicitly address pose ambiguities perform well when such ambiguities are eliminated by clearly visible anatomy. The design choices in E(3)-Pose provide the largest performance gains in cases with low visibility and high uncertainty, which is more common in clinical data.

L. Simulation study

Additional implementation details. We simulate stacks of 2D diagnostic slices (1×1mm pixels, 3mm slice thickness) in a specific target anatomical orientation (i.e., left→right, posterior→anterior, or inferior→superior). We simulate navigator volumes rapidly acquired before each slice from test volumes in Research-Fetal, by augmenting with 6mm isotropic resolution and a simulated spin history artifact based on the imaging plane parameters of the preceding slice. We simulate one stack in each orientation for each test volume, resulting in 168 total stacks. The number of slices per stack is adjusted for brain size as in current clinical practice, resulting in 23-40 slices per stack.

Recall from Appendix A that every slice is prescribed according to $\tilde{P}_k = \hat{T}_k P_k$, where \hat{T}_k is the estimated head pose in the preceding navigator volume. We compare \hat{T}_k returned

Table 9. **Ablation performance statistics on research data.** Mean \pm standard deviation statistics for rotation error ($^{\circ}$) and average absolute error (AAD, mm). Best score is in bold. * indicates statistical significance compared to E(3)-Pose ($p < 0.05$, pairwise Wilcoxon test).

	Trained on Research-Fetal				Trained on dHCP			
	Research-Fetal		dHCP		Research-Fetal		dHCP	
	Rot. error	AAD	Rot. error	AAD	Rot. error	AAD	Rot. error	AAD
E(3)-Pose (ours)	5.1 ± 2.6	3.0 ± 1.7	7.4 ± 3.6	3.7 ± 1.8	5.7 ± 3.6	3.4 ± 2.0	7.3 ± 3.4	3.7 ± 1.7
Standard CNN	$6.9 \pm 3.5^*$	$3.8 \pm 1.9^*$	7.5 ± 4.2	3.7 ± 2.0	$11.2 \pm 4.9^*$	$6.2 \pm 3.1^*$	7.5 ± 3.4	3.7 ± 1.7
no pseudovector	5.6 ± 2.4	3.2 ± 1.6	8.6 ± 3.3	4.2 ± 1.7	5.9 ± 3.0	3.4 ± 1.8	6.8 ± 3.2	$3.4 \pm 1.6^*$
$h(R) = e_y \oplus e_z$	5.3 ± 2.5	3.1 ± 1.5	6.8 ± 3.5	3.4 ± 1.6	5.9 ± 2.7	3.4 ± 1.6	7.5 ± 3.4	3.7 ± 1.7
$\mathcal{L}_\phi = \sum_{k \in \{x, y, z\}} \sin(\theta_k/2)$	4.9 ± 2.4	2.9 ± 1.5	7.2 ± 3.6	3.5 ± 1.6	5.9 ± 3.2	3.4 ± 1.8	7.3 ± 3.2	3.6 ± 1.5
geodesic loss	4.9 ± 2.1	2.9 ± 1.2	$6.5 \pm 3.8^*$	$3.3 \pm 1.7^*$	14.7 ± 38.1	6.8 ± 14.9	$73.8 \pm 84.4^*$	$24.9 \pm 27.4^*$
no artifact augmentation	5.1 ± 2.2	3.0 ± 1.4	$6.6 \pm 3.2^*$	$3.2 \pm 1.5^*$	$7.2 \pm 3.9^*$	$4.1 \pm 2.4^*$	7.6 ± 3.4	3.8 ± 1.6

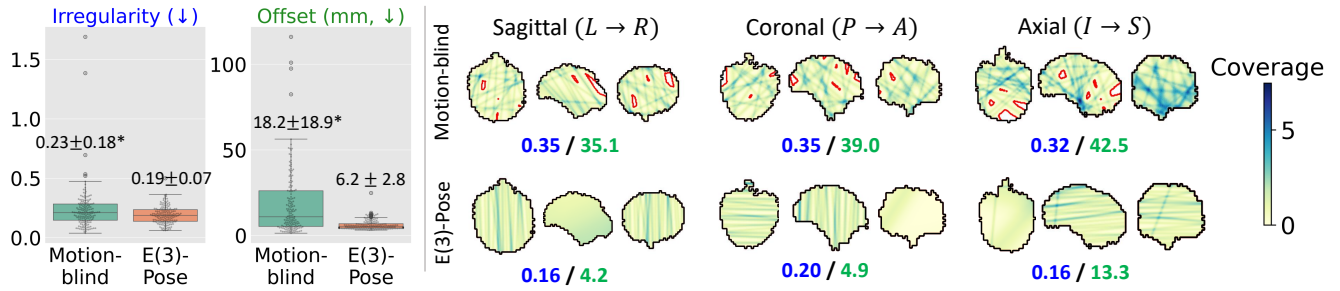


Figure 16. **Additional simulation results.** *Left:* Coverage irregularity and slice offset (mm) of diagnostic slice stacks obtained using motion-blind prescription and E(3)-Pose. Mean \pm standard deviation statistics are displayed. * indicates statistical significance ($p < 0.05$, pairwise Wilcoxon). *Right:* See Fig. 5 in the main paper for details. Here, coverage irregularity (blue) and slice offset (green, mm) metrics are respectively displayed.

by E(3)-Pose to that of “motion-blind” slice prescription, where we set $\hat{T}_k = T_{k=0}$ for all $k \geq 0$. To simulate inter-slice fetal brain motion for $k > 0$, we sample rigid motion $T_{k+1}T_k^{-1}$ from real fetal head motion trajectories, interpolated at time intervals of TR=3s to match the time between navigator volume acquisitions in the clinical setting [62]. Our motion trajectory dataset consists of full time-series from subjects in Clinical-Young, since increased uterine mobility in younger fetuses produces wider ranges of motion for our analysis. We follow prior work [75] in annotating motion trajectories in this dataset for the purposes of simulation. Specifically, we apply an existing fetal landmark detection algorithm to detect the fetal eyes and shoulders in every frame [14], manually correct algorithmically estimated landmarks, and finally compute the rigid motion between consecutive frames using detected landmarks.

We define the slice coverage distribution p_C over the underlying brain volume on a 1mm resolution grid as the sum of the Gaussian kernels representing the point spread function [39, 58, 75] of all slices in the stack. We then compute the coverage gap as the proportion of the brain volume where $p_C = 0$.

Additional evaluations. The primary aims of automated slice prescription are improvements in the spatial coverage of the brain and the radiological interpretability of the acquired

stack of slices. In the main paper, we partially quantify these qualities with the coverage gap and slice obliqueness, respectively. In this section, we include two additional metrics that further assess the diagnostic potential of the simulated slice stacks. First, because uneven spatial coverage is correlated with poor coverage quality and coverage gaps, we calculate the coverage irregularity $KL(p_C || p_U)$, where KL is the Kullback-Leibler divergence and p_U is the uniform distribution over the underlying brain volume. Second, since slice obliqueness only quantifies the rotational incoherence of slices within each stack, we also assess translational incoherence by computing the slice offset, i.e., the distance in mm between the center voxels of the GT and prescribed slices. Fig. 16 demonstrates that in our simulations, slice prescription with E(3)-Pose significantly improves both additional quantitative metrics of diagnostic potential, compared to motion-blind prescription.

M. Additional limitations and future work

Navigators dataset. Although we evaluate E(3)-Pose on data representative of automated slice prescription with respect to acquisition parameters and image quality, our analysis is limited to 9 pregnant participants who were recruited at the same institution and imaged on the same scanner. Furthermore, Navigators does not include sufficient representa-

tion of second-trimester fetuses. To investigate the broader applicability of our method for clinical translation, future work will extend our analysis on navigator volumes acquired in a larger, more diverse cohort of pregnant volunteers.

Symmetries. Beyond fetal imaging, it is interesting to investigate applications of our method under more relaxed reflectional and/or rigid symmetries [68], such as cardiac, lung, and adult brain imaging. Lastly, we expect that our method could be adapted to objects with more complex (e.g., n -fold rotations) symmetries (Appendix N).

N. Rotational object symmetries

In this work, we have demonstrated a rotation-equivariant framework for pose estimation of objects with reflectional symmetries, e.g., the fetal head. However, many real-world objects possess more complex symmetries. In this section, we sketch a method to estimate the pose of objects with N -fold rotational symmetries about an axis with an E(3)-CNN. We hypothesize that this will stabilize pose estimation in high-ambiguity situations, and will investigate the proposed method in future work.

Rotation parametrization. Recall that we denote the rotation of the object frame as R , the rotation parametrization as $h(R)$, and object symmetry group as G_{symm} . Here we consider the case where $G_{\text{symm}} = \{g_{\theta=2\pi(k/N)} | k = 1, \dots, N\}$ where $\theta = 2\pi(k/N)$ are the N -fold rotations in the plane of rotational symmetry. Let e_{\circlearrowright} be axis of rotational symmetry, and let $\text{parity}(N)$ be equal to the parity of the integer N . Then, we can train an E(3)-CNN to predict the following rotation parametrization:

$$\begin{aligned} h(R) &= e_x \oplus e_y \oplus e_z, \\ \text{s.t. } e_x &= D_{:, -N}^{l=N}(R), e_y = D_{:, N}^{l=N}(R) \text{ and } e_z = e_{\circlearrowright}, \\ \rho_h(g_r) &= D^{l=N}(g_r) \oplus D^{l=N}(g_r) \oplus M(g_r) \\ &= \rho_{\text{parity}(N)}^{l=N}(g_r) \oplus \rho_{\text{parity}(N)}^{l=N}(g_r) \oplus \rho_{\text{odd}}^{l=1}(g_r), \end{aligned} \quad (9)$$

where $D^l : \text{SO}(3) \rightarrow \mathbb{R}^{2l+1 \times 2l+1}$ is the Wigner-D matrix function of order l , and $D_{:, m}^l$ denotes its columns, indexed from $-l \leq m \leq l$. Columns of the Wigner-D matrices are irreducible tensors with irreducible Wigner-D matrix representations [20, 70]. Since $h(R)$ is parametrized in terms of irreducible tensors, it maintains equivariance under E(3). Therefore, the E(3)-CNN output is formulated as 1 vector and 2 irreducible tensors of order $l = N$ and parity $p = \text{parity}(N)$.

Invariance under object symmetry. Here we show that $h(R) = \rho_h(g_{\theta=2\pi(k/N)})h(R)$ for all $k = 1, \dots, N$. First, it is easy to see that $e_z = M(g_{\theta=2\pi(k/N)})e_z$ because in-plane rotations leave orthogonal vectors unchanged. Next, we show that $e_y = D^{l=N}(g_{\theta=2\pi(k/N)})e_y$

by showing that $\sum_{-N \leq m' \leq N} [e_y]_{m'} Y_{m=m'}^{l=N}(\theta, \phi) = \sum_{-N \leq m' \leq N} [D^{l=N}(g_{\theta=2\pi(k/N)})e_y]_{m'} Y_{m=m'}^{l=N}(\theta, \phi)$, where Y_m^l is the spherical harmonic function of degree l and order m , and the spherical coordinates (θ, ϕ) refer to the polar and azimuthal angles, respectively. The same reasoning can be applied to e_x .

Let $(\theta, \phi) \xrightarrow{R} (\theta', \phi')$ define the spherical coordinate transformation under rotation $R \in \text{SO}(3)$. We observe that

$$\begin{aligned} &\sum_{-N \leq m' \leq N} [e_y]_{m'} Y_{m=m'}^{l=N}(\theta, \phi) \\ &= \sum_{-N \leq m' \leq N} D_{m', N}^{l=N}(R) Y_{m=m'}^{l=N}(\theta, \phi) \\ &= Y_{m=N}^{l=N}(\theta', \phi') \end{aligned} \quad (10)$$

where we have used the property $Y_m(\theta', \phi') = \sum_{-l \leq m' \leq l} D_{m'm}^l(R) Y_{m'}^l(\theta, \phi)$.

Similarly, we have

$$\begin{aligned} &\sum_{-N \leq m' \leq N} [D^{l=N}(g_{\theta=2\pi(k/N)})e_y]_{m'} Y_{m=m'}^{l=N}(\theta, \phi) \\ &= \sum_{-N \leq m' \leq N} [D^{l=N}(g_{\theta=2\pi(k/N)})D_{:, N}^{l=N}(R)]_{m'} Y_{m=m'}^{l=N}(\theta', \phi') \\ &= \sum_{-N \leq m' \leq N} D_{m', N}^{l=N}(g_{\theta=2\pi(k/N)}R) Y_{m=m'}^{l=N}(\theta, \phi) \\ &= Y_m^{l=n}(\theta' + \frac{2\pi k}{N}, \phi') = e^{iN2\pi(k/N)} Y_{m=N}^{l=N}(\theta', \phi') \\ &= e^{i2\pi k} Y_{m=N}^{l=N}(\theta', \phi') = Y_{m=N}^{l=N}(\theta', \phi') \\ &= \sum_{-N \leq m' \leq N} [e_y]_{m'} Y_{m=m'}^{l=N}(\theta, \phi) \end{aligned} \quad (11)$$

where we use the properties $D^l(R_1)D^l(R_2) = D^l(R_1R_2)$ for any $R_1, R_2 \in \text{SO}(3)$ and $Y_l^m(\theta_1 + \theta_2, \phi) = e^{im\theta_2} Y_l^m(\theta_1, \phi)$.

Training. We aim to maintain symmetry invariance in our training objective. To this end, any standard regression loss (e.g., \mathcal{L}_1 or \mathcal{L}_2 norm) on the error term $h(R) - [\hat{e}_x \oplus \hat{e}_y \oplus \hat{e}_z]$ between the GT rotation parametrization and the E(3)-CNN output, respectively, satisfies this condition.

Inference. Since Wigner-D matrices are a Fourier basis for functions defined on $\text{SO}(3)$, the E(3)-CNN output represents a likelihood function P over $\text{SO}(3)$, where $P(R')$ is monotonically related to the inner product between $h(R')$ and $[\hat{e}_x \oplus \hat{e}_y \oplus \hat{e}_z]$ [42]. It is possible to sample from P by querying values on a predefined equivolumetric grid over $\text{SO}(3)$ [27]. Indeed, if the E(3)-CNN output $[\hat{e}_x \oplus \hat{e}_y \oplus \hat{e}_z]$ is equal to $h(R)$, then P is nonzero and uniformly distributed over the set of poses that are symmetrically equivalent to R , and zero elsewhere.